SLAC-PUB-12276

January 2007

Fallback and Black Hole Production in Massive Stars

Weiqun Zhang[1], S. E. Woosley[2], and A. Heger[2,3]

ABSTRACT

The compact remnants of core collapse supernovae - neutron stars and black holes - have properties that reflect both the structure of their stellar progenitors and the physics of the explosion. In particular, the masses of these remnants are sensitive to the density structure of the presupernova star and to the explosion energy. To a considerable extent, the final mass is determined by the "fallback", during the explosion, of matter that initially moves outwards, yet ultimately fails to escape. We consider here the simulated explosion of a large number of massive stars (10 to 100 $M_\odot$) of Population I (solar metallicity) and III (zero metallicity), and find systematic differences in the remnant mass distributions. As pointed out by Chevalier (1989), supernovae in more compact progenitor stars have stronger reverse shocks and experience more fallback. For Population III stars above about 25 $M_\odot$ and explosion energies less than 1.5×10^{51} erg, black holes are a common outcome, with masses that increase monotonically with increasing main sequence mass up to a maximum hole mass of about 35 $M_\odot$. If such stars produce primary nitrogen, however, their black holes are systematically smaller. For modern supernovae with nearly solar metallicity, black hole production is much less frequent and the typical masses, which depend sensitively on explosion energy, are smaller. We explore the neutron star initial mass function for both populations and, for reasonable assumptions about the initial mass cut of the explosion, find good agreement with the average of observed masses of neutron stars in binaries. We also find evidence for a bimodal distribution of neutron star masses with a spike around 1.2 $M_\odot$ (gravitational mass) and a broader distribution peaked around 1.4 $M_\odot$.

Subject headings: supernovae: general – black hole physics – stars: neutron – hydrodynamics

---

[1] Kavli Institute for Particle Astrophysics and Cosmology, Stanford University, P.O. Box 20450, MS 29, Stanford, CA 94309; Chandra Fellow

[2] Department of Astronomy and Astrophysics, University of California, Santa Cruz, CA 95064

[3] T6 Los Alamos National Laboratory, Los Alamos, New Mexico

Submitted to Astrophysical Journal

Work supported in part by US Department of Energy contract DE-AC02-76SF00515

1. INTRODUCTION

Colgate (1971) first introduced the idea of fallback in supernovae, attributing it to accretion in the rarefaction behind the outgoing shock. Chevalier (1989) discussed fallback in supernovae extensively and emphasized that greater accretion would occur in compact progenitors. For SN 1987A, a blue supergiant, Chevalier estimated a relatively large fallback mass of $\sim$0.1 $M_\odot$, and, for the more common Type II supernovae from red supergiants, a value roughly 100 times smaller. He also found, using self-similarity arguments, that the accretion rate at late times when expansion dominated should scale as $t^{-5/3}$, and emphasized the role of the reverse shock in fallback (see also Colgate 1988). Woosley & Weaver (1995) studied fallback numerically in a variety of supernovae with different masses and compositions, and emphasized black hole formation as an important outcome for stars of higher mass and lower metallicity, with important ramifications for their nucleosynthesis. MacFadyen et al. (2001) studied fallback numerically in a 25 $M_\odot$ supernova with varying explosion energy and discussed the relevance of fallback for producing gamma-ray bursts.

Thus far, however, there has been no systematic study of fallback in stars with a very low metal content to determine the properties of gravitational remnants that might have existed following a first generation of stars of varying mass. It has also been some time since the remnant masses of solar metallicity stars were systematically explored (Timmes et al. 1996), and no such studies have included the effects of mass loss. Calculations of fallback can be greatly influenced by the way the inner boundary is handled (MacFadyen et al. 2001). This is particularly true in cases where a piston or reflecting inner boundary has been used to simulate the explosion and is still present in the calculation at late times (e.g., Woosley & Weaver 1995). As we shall see, for modern supernovae that are red giants when they die, the error introduced by this artificial inner boundary is small, but it can become appreciable for zero metallicity stars with a much larger amount of fallback.

Since the material that falls back must be subtracted from the element production for a given star, our results are also relevant for calculations of nucleosynthesis and (radioactive-powered) light curves.

We do not study fallback in stars above 100 $M_\odot$leave out the effects of rotation. Above 100 $M_\odot$ and below 260 $M_\odot$, non-rotating stars encounter the pair instability and either lose their outer layers before explosion (pulsational pair instability) or explode completely without fallback. Above 260 $M_\odot$, they collapse to black holes (Heger & Woosley 2002). We also study here only single stars, not binaries. The complications introduced by rotation and binary membership could be included in future studies.

2. INITIAL MODELS

The supernova models studied here are taken from two recent surveys by Heger & Woosley (2007) and Woosley & Heger (2007). In each case, stars of various masses and metallicities were evolved using the Kepler code (Weaver et al. 1978; Woosley et al. 2002) through all stable stages of nuclear burning until their iron cores became unstable to collapse. The stars were then exploded using pistons located at or near the edge of their iron cores. For a discussion of how the piston was located and moved, and for further details of these explosion models, see the two reviews.

The first of these surveys examined the evolution and simulated explosion of approximately 120 massive stars with masses in the range 10 - 100 $M_\odot$ and zero initial metallicity (hence Population III; Table 1). Heger and Woosley explored twelve different choices of explosion energy and piston location for each mass. While results are given for all of them in the tables, the discussion here focuses on just five. The model names are given by a capital letter "Z", for "zero" metallicity, followed by a letter indicating the piston location and explosion energy. Four of these, Series ZB, ZD, ZG, and ZJ, had the piston located at that point in the star where the entropy equals $4.0\,k_{\rm B}$/baryon (typically this occurs at the base of the oxygen burning shell) and kinetic energies of 0.6, 1.2, 2.4, and 10 B respectively (henceforth 1 B = 1 Bethe = 10^{51} erg). Series P had the piston located deeper in, at the edge of the deleptonized core (where the electron mole number, Y_e, drops precipitously below 0.5 due to electron capture) and had an explosion energy of 1.2 B. Note that the explosion energies quoted here are not the energy input by the piston, but rather the kinetic energy of the ejecta at infinity.

The second survey treated a somewhat coarser grid of stellar masses (31 stars) with solar metallicity and masses in the range 12 - 100 $M_\odot$ (Table 2). This survey is more appropriate to supernovae today in the Milky Way Galaxy. Greatest attention is paid here to Series SA, which had the piston at the place in the star where the entropy per baryon, $S/N_A k$, equals 4.0 and an explosion energy of 1.2 B. Except for metallicity effects then, series ZD and SA are directly comparable. Three other explosion models were also considered: SB which had the piston at the entropy = 4.0 point but had an explosion energy of 2.4 B; SC, with the piston at the edge of the iron core (mass fraction of nuclei heavier than chromium greater than 50%) and an explosion energy of 1.2 B; and SD, with the piston at the edge of the iron core and an explosion energy of 2.4 B.

Models SC are thus the solar metallicity counterparts of Models ZP but with a slight difference. The ZP models put the piston at the edge of the deleptonized core; the SC models, at the edge of the iron core. The difference between these two cores in a given model is usually quite small and we do not think it had a major effect on the outcome.

Tables 1 and 2 give an overview of these presupernova models. See also Heger & Woosley (2007) and Woosley & Heger (2007). For the solar case, a few additional models were computed at low and high mass using the same code and physics as the original surveys. The tables give the initial mass of the star, its final mass (for the Pop III stars, this is identical to the initial mass), the mass of the location where an entropy of $S/N_Ak = 4.0$ is reached ($M_{\mathrm{S=4}}$), the size of the core where extensive electron capture has occurred (Y_e core), the binding energies outside these two cores (binding energy minus internal energy; $BE_{\mathrm{Ye\ core}}$, $BE_{\mathrm{S=4}}$), and the final radius of the star (R_{eff}). In the R_{eff} column, "WNL" indicates a hydrogen-rich Wolf-Rayet (WR) star and "WC"/"WO" indicate early-type hydrogen-free WR stars. Such WR stars have optically thick winds with a photospheric "effective radius" located in this wind regime. Among the hydrogen-free WR stars, we found only the carbon-rich and oxygen-rich subtypes (WC and WO) at presupernova, but no early-type hydrogen-free WR stars that only display the pure CNO-processed N-rich He layer (WNE stars). There may be a very small transition regime between 40 and 45 $\mathrm{M}_{\odot}$where such WNE stars occur. At 45 $\mathrm{M}_{\odot}$the early-type WR regime starts by making WO stars. This is because material from a late helium burning stage in which oxygen dominates over carbon is exposed to the surface. At initial masses above $\sim$ 60 $\mathrm{M}_{\odot}$ carbon dominates over oxygen at the time the stars explodes. The final mass of the star becomes smaller having lower WR mass loss rates at the end and the stars lose mass from earlier phases of helium core bunring. Both effects increase the *final* carbon-to-oxygen ratio at the surface.

3. CALCULATIONS

The supernova models were linked from the Kepler code, in which they were initially calculated, to the Pangu code 100 s after the shock wave had been initiated. This typically corresponded to a time when explosive nucleosynthesis had ended and the outgoing shock was just exiting the core of helium and heavy elements, before it had encountered any appreciable fraction of the hydrogen envelope. The reverse shock had thus not yet developed and, for the explosion energies considered, no fallback had yet occurred.

Pangu is a one-dimensional hydrodynamics code based on the second-order semi-discrete finite-difference central scheme of Kurganov & Tadmor (2000). Time evolution is carried out by a third-order total variation diminishing Runge-Kutta method (Shu & Osher 1989). We extended the scheme to spherical coordinates based on the conservative form of hydrodynamics equations. The treatment of spherical coordinates is the same as that in the RAM code (Zhang & MacFadyen 2006). In spherical coordinates, extra source terms are added to the equations. Geometric correction to the surface area and volume of discretized numerical cells is applied when the numerical flux is used to update conserved variables (density, momentum and total energy) in the cells.

Gravity is implemented as source terms of the hydrodynamics equations. A point mass is placed at the center of the grid. The gravitational force at a grid point is calculated from the enclosed mass, which includes the central point mass and mass of the material on the computational grid. The central point mass is being updated by keeping track of the mass flux across the inner boundary.

An outflow boundary condition is used at the inner boundary. That is, the ghost cells are simple duplicates of the first numerical cell on the grid. This type of boundary is very simple to implement. A potential problem of essentially any numerical boundary is small errors at the boundary could accumulate and affect the calculation. To avoid the problem, one should make sure that the flow across the boundary is supersonic. Thus the information at the boundary cannot propagate outwards and affect the upstream fluid. In our calculations, the inner boundaries are chosen to be small enough to ensure the supersonic condition. However, it could be expensive to use a very small radius for the inner boundary because of the constrain of the Courant-Friedrichs-Lewy condition. Fortunately, the sound speed at the inner boundary is decreasing during fallback due to the decrease of temperature, whereas the infall velocity is increasing during fallback. Therefore the sonic point is moving outwards over the time. Taking advantage of the above phenomenon, our calculations are performed in two steps to save computing time. In the first step, the numerical grid has an inner boundary at $r = 10^9\,\mathrm{cm}$, which is also the inner boundary of the initial Kepler models, and an outer boundary at $r = 10^{14}\,\mathrm{cm}$. A logarithmic grid with 1000 zones is used for the r-direction. The region outside the star is filled with a low density medium with a pressure of $p = 10\,\mathrm{dyn\,cm^{-2}}$, a density of $\rho = 10^{-12}\,\mathrm{g\,cm^{-3}}$ and zero velocity. The calculation is run to $t = 10^5\,\mathrm{s}$. Then the model is remapped to a new grid for the second step of calculations. For red giants in which the forward shock could have moved beyond the outer boundary at $r = 10^{14}\,\mathrm{cm}$ already at $t = 10^5\,\mathrm{s}$, the link to the second step is at an earlier time (e.g., $t = 5 \times 10^4\,\mathrm{s}$) so that the forward shock still presents at the second step. The new grid also has 1000 logarithmic zones, but the boundaries are at $r = 10^{10}\,\mathrm{cm}$ and $r = 10^{16}\,\mathrm{cm}$. Again the outside medium is set to a constant state with a pressure of $p = 10\,\mathrm{dyn\,cm^{-2}}$, a density of $\rho = 10^{-12}\,\mathrm{g\,cm^{-3}}$ and zero velocity. The second step of the calculation is run to at least $t = 10^6\,\mathrm{s}$. Then the simulation continues till the accretion rate is below $10^{-8}\,\mathrm{M_\odot\,s^{-1}}$ or it has reached $t = 2.0 \times 10^6\,\mathrm{s}$.

4. RESULTS

4.1. Fallback in Population III Supernovae

Two distinguishing properties of Pop III stars are that they do not lose appreciable mass and they typically have much more compact envelopes than modern stars. Most of them die as hot blue stars. In some of the more massive stars, however, penetration of the convective helium burning core into the hydrogen envelope leads to the enrichment of the latter with super-solar abundances of carbon and nitrogen. Hydrogen shell burning by the CNO cycle then expands the star to supergiant proportions. Another special case is stars around $100\,\mathrm{M}_\odot$ which begin to encounter the pulsational pair instability. Strong pulses lead to the ejection of the entire hydrogen envelope and even parts of the helium core before the final core collapse (e.g., Heger & Woosley 2002). This weakens the reverse shock in such stars.

In the usual case, however, the explosion of Pop III stars is accompanied by a stronger reverse shock and much more fallback than in their solar counterparts. Since mass loss is negligible in these stars, higher main sequence mass implies a monotonically increasing helium core mass when the star dies, and along with it the potential for making more massive compact remnants, especially if the explosion energy is small. This is particularly interesting since several current simulations of primordial star formation (e.g., O'Shea & Norman 2006) predict rather high initial masses for these first stars. While not studied here, it is expected that still more massive stars (i.e., much above $100\ \mathrm{M}_\odot$), will encounter an increasingly violent pair instability leading to the complete disruption of the star and, eventually, above about $260\ \mathrm{M}_\odot$, the direct production of massive black holes without an initial supernova explosion (Heger & Woosley 2002). These limiting masses would be reduced by rotation.

4.1.1. Hydrodynamics in a Representative Case

Fig. 1 shows the pressure, density, and velocity profiles at 100 s, 200 s, and 1000 s as calculated in a typical Pop III model, Z25D, using both Pangu and Kepler. Both the forward and reverse shocks are clearly visible in the pressure and velocity plots. The reverse shock forms as the expanding helium core runs into the star's hydrogen envelope (where the quantity ρr^3 increases; Woosley & Weaver 1995) and is decelerated. The hydrogen envelope in the presupernova star had its base at 1.5×10^{10} cm. With time the reverse shock moves inwards in mass but outwards in radius. Starting at the edge of the helium core at $7.6\,\mathrm{M}_\odot$, by 1000 s the reverse shock has moved into $3.3\,\mathrm{M}_\odot$. The forward shock at this time is located at $19.19\,\mathrm{M}_\odot$ and will shortly exit the star.

In the part of the star that is sonically disconnected from the origin, the results of Kepler and Pangu are in very good agreement. As time passes, however, there is an increasing discrepancy near the origin where Pangu gives much higher collapse speeds than Kepler, since the latter increasingly feels the effect of the reflecting inner boundary held fixed at 1.0×10^9 cm. The inner boundary in Pangu is also located at 1.0×10^9 cm, but matter can flow through it without deceleration. The sonic radius at 1000 s is located at 3.27×10^{10} cm where the sound speed is $488\,\mathrm{km\,s^{-1}}$.

Fig. 2 gives the accretion rate as a function of time calculated by Pangu for this model. There are clearly four stages to the accretion: 1) an early rapid accretion of material that failed to achieve escape speed on the first try; 2) a decline in accretion rate to an asymptotic dependence on $\mathrm{t}^{-5/3}$ as appropriate for free expansion Chevalier (1989); 3) a greatly enhanced fallback as the reverse shock arrives at the core at 1.17×10^4 s; and 4) a final stage of free expansion.

The final value of the remnant masses from Pangu can be determined in two ways. After a sufficiently long time (i.e., a while after the reverse shock has arrived at the center), the inner part of the supernova will approach its asymptotic behavior. Thus, the profiles of pressure, density and velocity near the center are very simple for the last dump of the simulation. Both density and pressure have a negative gradient. The velocity is negative near the center and increases monotonically outwards. In the first method, a lower bound and upper bound of the final remnant mass can be estimated from the last dump. All material with a negative velocity will fall into the center. This gives us a lower bound estimate of the final remnant mass. All material with a velocity larger than the escape velocity will be able to escape. This gives us an upper bound estimate of the mass. Our first estimate is the average of the two bounds. The second estimate is based on the asymptotic behavior of the accretion rate, $\dot{M} \sim t^{-5/3}$. Using the point mass and accretion rate at the last dump of the simulation, we can get the second estimate by a simple analytic integration. For most models, the two estimates are almost the same. For example, the difference is less than $0.01\ \mathrm{M}_\odot$ in 958 out of 1440 Z-series and 123 out of 124 S-series models. This gives us more confidence about our results. In principle, the two estimates should be identical provided that the simulation is run long enough. To determine which estimate is more accurate, we did the two estimates using earlier dumps. We found that the second estimate was generally more accurate. In this paper, we will use the values of the second estimate. Tables 3 and 4 show the results of the final remnant masses calculated by Pangu. In the end, Pangu gave a remnant mass of $4.157\,\mathrm{M}_\odot$ for this star (Z25D) whereas the corresponding calculation with Kepler gave $2.173\,\mathrm{M}_\odot$.

4.1.2. Remnant Masses for the Pop III Survey

Fig. 3 gives the remnant masses for the Population III survey. Fig. 4 shows the results for lower mass stars ($< 25\,\mathrm{M}_\odot$) of the survey. Above about 35 $\mathrm{M}_\odot$ the results are influenced by the possibility of primary nitrogen production in the star (Heger & Woosley 2007). For such massive stars, the entropy barrier separating the outer extent of the convective core during helium burning is not sufficient to prohibit mixing with the hydrogen envelope with its very weak burning shell (this phenomenon does not occur in non-rotating stars of solar metallicity). The mixing of hydrogen and hot carbon leads to the production of nitrogen which is convected throughout most of the envelope. With the new large CNO abundance, nuclear energy generation is increased and the star eventually expands to red supergiant proportions. Stars that do not make nitrogen in this way stay compact. As Fig. 3 shows, the result is two branches of remnant masses.

Figs. 5, 6, and 7 show the distribution of remnant masses for primordial supernovae with explosion energies 0.6 B, 1.2 B, and 2.4 B for a piston located at the $S/N_Ak = 4$ point. Fig. 8 shows a similar remnant mass distribution for a piston located at the edge of the deleptonized core, for an explosion energy of 1.2 B. The systematics of these results are discussed in § 5.

4.2. Fallback in Population I Supernovae

Massive Pop I stars differ from Pop III stars in that they develop strong hydrogen burning shells and become red supergiants. Their envelopes are thus, globally speaking, less tightly bound than in Pop III stars, and also have different profiles of ρr^3 as a function of radius. Consequently, reverse shocks are weaker in red supergiants, as noted by Chevalier (1989) and Woosley & Weaver (1995), and their remnant masses are smaller. Above about 35 $\mathrm{M}_\odot$ solar metallicity stars lose their envelopes to winds during the red giant stage and become Wolf-Rayet stars. The Wolf-Rayet stars lose further mass so that, for example, a star with an initial mass of $100\,\mathrm{M}_\odot$ dies with a mass of only $6\,\mathrm{M}_\odot$. Such light stars obviously cannot leave behind very massive black holes and, in fact, tend to leave neutron stars.

Fig. 9 shows the remnant masses expected for solar metallicity. These masses are influenced both by the decreased amount of fallback that happens in the reverse shock in red supergiants and by the mass loss before the explosion, especially above $40\,\mathrm{M}_\odot$.

Fig. 10 shows the distribution of neutron star *gravitational* masses for the solar metallicity survey. The properties of these are sensitive to the placement of the piston as well as its energy and the figure is for a piston location at the $S/N_Ak = 4$ point near the base of the oxygen shell and an explosion energy of 1.2 B. The insert shows the distribution of *baryonic* masses of black holes, on a logarithmic scale on the x-axis. The main figure and the insert are normalized to add up to 100 % together (all remnants; see caption of Fig. 10 for details). Fig. 11 shows the same diagram of remnant mass distribution for a piston located deeper in the star, at the edge of the iron core.

5. REMNANTS

5.1. Gravitational and Baryonic Masses

The fallback calculations described above and as summarized in Tables 3 and 4 give the *baryonic* remnant masses. For neutron stars especially, a significant fraction of this mass becomes binding energy and is radiated away in the form of neutrinos. This fraction can be estimated if the binding energy of the neutron star is known, but is dependent upon the nuclear equation of state employed. Here the estimate of Latimer & Prakash (2002) is adopted:

$$BE = \frac{3}{5}\beta\left(1-\frac{1}{2}\beta\right)^{-1}, \qquad \beta = \frac{\mathrm{G}M_{\mathrm{remnant}}}{R_{\mathrm{remnant}}\mathrm{c}^2} \tag{1}$$

where G is the gravitational constant, M_{remnant} the gravitational mass of the remnant, R_{remnant} the radius of the remnant, and c the speed of light. Latimer & Prakash (2002) recommend a radius of $\sim 12\,\mathrm{km}$. This equation can then be solved to give a remnant mass as a function of baryonic mass, M_{baryon}:

$$M_{\mathrm{remnant}} = M_{\mathrm{baryon}}\left(1+\frac{3}{5}\frac{\mathrm{G}M_{\mathrm{baryon}}}{R_{\mathrm{remnant}}\mathrm{c}^2}\right)^{-1}. \tag{2}$$

Here, two choices of maximum neutron star mass are employed, 1.7 $\mathrm{M}_\odot$ and 2.0 $\mathrm{M}_\odot$. The limiting baryonic mass for which such heavy neutron stars are made is then computed from

$$M_{\mathrm{baryon}} = M_{\mathrm{remnant}}\left(1-\frac{3}{5}\frac{\mathrm{G}M_{\mathrm{remnant}}}{R_{\mathrm{remnant}}\mathrm{c}^2}\right)^{-1}. \tag{3}$$

For example, a maximum gravitational mass of 2.0 $\mathrm{M}_\odot$ implies a maximum baryonic mass of $2.35\,\mathrm{M}_\odot$. For baryonic masses above that limit, a black hole forms. Here any effects due to rotation are neglected.

Remnants that collapse to black holes may also lose an appreciable fraction of their baryonic mass in the formation process, but unlike neutron stars, that fraction depends not just on the final state but on the formation process. If the black hole forms promptly from a big collapsing core, bypassing any neutron star stage, and if the fallback of matter contributing to its mass is small or essentially spherically symmetric, very little rest mass is radiated away in form of neutrinos. The gravitational mass approximately equals the baryonic mass. On the other hand, one could first form a massive neutron star that cools, radiating away approximately 20 % of its rest mass before it collapses. If the black hole is a rapidly rotating Kerr black hole, the binding energy of the last stable orbit is 42.3 % of the rest mass. If the disk is hot enough and not advection dominated, this energy is radiated away. Depending on the size of the black hole, its rotation, and how much mass it accreted through a cooling disk and at what rotation rate of the black hole that occurred, the gravitational mass could be some 20 % to 40 % smaller than the baryonic mass.

For simplicity here, we assume that the gravitational mass of any black hole remnant equals the mass of the baryons that made it with no correction for neutrino losses. It should be kept in mind, however, that this is actually an upper limit to the mass of the black hole. Perhaps more realistically, the binding energy of the heaviest stable neutron star, about 0.25 $M_\odot$, should be subtracted from all our black hole remnant masses, assuming that, along the way, each black hole was formed from a protoneutron star that reached its maximum mass, radiated its binding energy, and then collapsed. In the spirit of the rest of the paper, all effects due to rotation are neglected.

5.2. The Corrected Remnant Mass Distribution

The distribution of remnant masses is obtained by linear interpolation of the remnant masses among the different initial masses. The result is then integrated over a Salpeter initial mass function (IMF) with exponent -1.35. The resulting mapping into bins is exact. A bin width of $0.025\,M_\odot$ is used. The averages and standard deviations (Table 5) are computed from this distribution. For the black holes, the average logarithmic mass (geometric mean) is also given. The column "BH (%)" gives the fraction of remnants, from the mass range considered, that are black holes. The fraction of neutron stars is one minus that number.

To round out the table, remnant masses for main sequence stars lighter than the $12\,M_\odot$ considered by Woosley & Heger (2007) and the 10 $M_\odot$ considered by Heger & Woosley (2007) were estimated. Presupernova models of resulting from 10 and 11 solar mass solar metallicity stars were computed using the same physics and codes as described in the review. Because such stars result in a degenerate core surrounded by thin layers of heavy elements, it is reasonable to expect fallback to be negligible in the explosion. The (baryonic) remnant masses were just taken to be S/N_Ak=4.0 masses of the presupernova stars, $1.37\,M_\odot$ for the $11\,M_\odot$ star and $1.35\,M_\odot$ for the $10\,M_\odot$. The same 1.35 $M_\odot$ value was taken to characterize all stars down to $9.1\,M_\odot$, the assumed transition to super-asymptotic giant branch (SAGB) stars (Poelarends *et al.* 2007). For the piston located at the Fe core, a remnant mass of

$1.32\,\mathrm{M}_\odot$ was assumed for the $11\,\mathrm{M}_\odot$ star and lighter stars.

For the zero metallicity stars, the remnant characteristics of the $10\,\mathrm{M}_\odot$ were assumed to hold down to the SAGB limit for Z = 0 stars, taken here to be $9.5\,\mathrm{M}_\odot$.

6. DISCUSSION AND CONCLUSIONS

Table 6 gives the statistical characteristics of sets of compact remnants extracted from an IMF-averaged distribution of supernovae of the two populations. Here a Salpeter IMF is assumed over the entire mass range examined, $9 \lesssim \mathrm{M}/\mathrm{M}_\odot \lesssim 100$. The error bars represent a one-sigma deviation in the distribution. Different choices for the IMF could be explored by others using the values in Tables 3 and 4. For the black hole masses, the logarithmic average as well as the arithmetic average might be of interest and both are given. The statistical results depend not only on the physics of the explosion (piston mass and energy), but also on the assumed maximum mass of the neutron star. Obviously, the heavier that maximum mass, the fewer the number of black holes.

In general, the observed trends follow expectation. More energetic explosions eject more matter, experience less fallback, and make lighter compact remnants. Even the lowest energy explosions considered, 0.3 B, eject most of the hydrogen envelope of all Pop III stars. Thus a supernova-like display can be expected in all cases - though the event may be very faint if the radius is small and no ^{56}Ni is ejected (Heger & Woosley 2007; Scannapieco et al. 2005). The mass of the black hole in these low energy explosions approaches that of the helium core of the presupernova star (Fig. 3), e.g., $\sim$ 10 $\mathrm{M}_\odot$ in a 25 $\mathrm{M}_\odot$ supernova and $\sim$45 $\mathrm{M}_\odot$ in a 100 $\mathrm{M}_\odot$ star. The average black hole mass from a generation of such zero-metal stars ranges from about 6 to 10 $\mathrm{M}_\odot$ if one excludes hyper-energetic explosions (5 B and more) and very low energy ones. There is great variation about this mean though, and hole masses up to $40\,\mathrm{M}_\odot$ are quite possible. The fraction of black hole remnants is also high, typically 20 - 50% and possibly as great as 90%. If modern supernovae can be taken as a guide, the results for $S/N_A k = 4$, 1.2 B case (Model SA) may be most realistic (Woosley & Heger 2007).

The fraction of remnants that are black holes is clearly smaller for modern (i.e., solar metallicity) stars, and the average mass of those holes is smaller. The actual value is sensitive to the values adopted for the maximum neutron star mass and explosion energies, but percentages in the range 10 - 25% are reasonable. Explosion energies as great as 2.4 B would probably give Type II supernova light curves that are too bright (Woosley & Heger 2007). Typical black hole masses are around 3 $\mathrm{M}_\odot$ unless the explosion energy is very low.

Experimental estimates for the average black hole mass are hard to find, and it must be kept in mind that accurate values for the black hole mass can only come from binaries where the evolution might have been influenced by mass exchange. Rotation can also affect the relation between helium core mass and main sequence mass and possibly lead to larger black holes. There is also a predisposition to find massive black holes since it is the mass that is taken as an indicator that the object is not a neutron star. Still it is interesting that rather large values for black hole masses have been reported in systems that presumably were not particularly metal poor (Remillard & McClintock 2006; Harrison et al. 2007). Either such systems have experienced an atypical evolution (either of the black hole progenitor star or the black hole itself after it was born) or the explosion energies are substantially less than what one commonly takes for Type II supernovae.

Much better experimental calibrations are available for neutron star masses, though one still must be concerned about the favored selection of objects in close binary systems. The average neutron star masses for solar metallicity stars in Table 6 range from 1.33 to 1.47 $\mathrm{M}_{\odot}$. This is to be compared with, e.g., estimates by Thorsett & Chakrabarty (1999) of 1.35 ± 0.04 $\mathrm{M}_{\odot}$ for 21 radio pulsars. While the agreement of the averages is impressive, it is also noteworthy that many neutron stars in our calculated data set have masses outside this range. In fact the lightest neutron star in the sample has a gravitational mass of 1.16 $\mathrm{M}_{\odot}$ for the $S = 4$ set and $1.08\,\mathrm{M}_{\odot}$ for the iron core set. There are also numerous cases of neutron stars with gravitational masses around the maximum mass limit.

Two major deficiencies of the current study is that it does not include the effects of rotation or of binary interaction. The former will tend to increase the mass of the remnants for a given main sequence star since it leads to a larger helium core mass. The latter may lead to reduced masses for remnants, especially if the parent star loses its envelope early on to a companion and loses a lot more mass as a Wolf-Rayet star. Both effects could be included in future studies. It would also be useful to explore a wider range of explosion energies for the solar metallicity stars. We plan such a survey, with mass and energy resolution more like the Pop III survey presented here, in the very near future.

WZ has been supported by NASA through Chandra Postdoctoral Fellowship PF4-50036 awarded by the Chandra X-Ray Observatory Center. SW has been supported by the NSF (AST 0206111) and the DOE SciDAC Program (DOE DE-FC-02-01ER41176 and DOE DE-FC-02-06ER41438). AH carried out this work under the auspices of the National Nuclear Security Administration of the U.S. Department of Energy at Los Alamos National Laboratory under Contract No. DE-AC52-06NA25396, and was supported by the DOE Program for Scientific Discovery through Advanced Computing (SciDAC; DE-FC02-01ER41176).

REFERENCES

Chevalier, R. A. 1989, ApJ, 346, 847

Colgate, S. A. 1971, ApJ, 163, 221

Colgate, S. A. 1988, Supernova 1987A in the Large Magellanic Cloud, 341

Harrison, T. E., Howell, S. B., Szkody, P., & Cordova, F. A. 2007, AJ, 133, 162

Heger, A., & Woosley, S. E. 2002, ApJ, 567, 532

Heger, A., & Woosley, S. E. 2007, ApJ, in preparation

Kurganov, A., & Tadmor, E. 2000, J. Comput. Phys., 160, 241

MacFadyen, A. I., Woosley, S. E., & Heger, A. 2001, ApJ, 550, 410

Lattimer, J. M., & Prakash, M., 2002, ApJ, 550, 426

O'Shea, B. W., & Norman, M. L. 2006, ApJ, in press; astro-ph/0607013

Poelarends, A.J.T., Herwig, F., Langer, N., Heger, A. 2007, ApJ, in preparation.

Remillard, R. A., & McClintock, J. E. 2006, ARA&A, 44, 49

Scannapieco, E., Madau, P., Woosley, S., Heger, A., & Ferrara, A. 2005, ApJ, 633, 1031

Shu, C.-W., & Osher, S. 1989, J. Comput. Phys., 83, 32

Thorsett, S. E., & Chakrabarty, D. 1999, ApJ, 512, 288

Timmes, F. X., Woosley, S. E., & Weaver, T. A. 1996, ApJ, 457, 834

Weaver, T. A., Zimmerman, G. B., & Woosley, S. E. 1978, ApJ, 225, 1021

Woosley, S. E., & Weaver, T. A. 1995, ApJS, 101, 181

Woosley, S. E., Heger, A., & Weaver, T. A. 2002, Reviews of Modern Physics, 74, 1015

Woosley, S. E., & Heger, A. 2007, Physics Reports, in press

Zhang, W., & MacFadyen, A. I. 2006, ApJS, 164, 255

This preprint was prepared with the AAS LaTeX macros v5.0.

Table 1: Summary of $Z = 0$ Presupernova Model Data

mass ($M_\odot$)	$M_{\rm S=4}$ ($M_\odot$)	Y_e core ($M_\odot$)	$BE_{\rm Ye\ core}$ (B)	$BE_{\rm S=4}$ (B)	$R_{\rm eff}$ ($R_\odot$)
10.0	1.28	1.27	0.09	0.09	62
10.2	1.38	1.18	0.27	0.04	38
10.4	1.32	1.18	0.34	0.11	34
10.5	1.41	1.20	0.34	0.07	27
10.6	1.40	1.20	0.30	0.06	21
10.7	1.41	1.19	0.35	0.08	20
10.8	1.34	1.17	0.39	0.13	19
10.9	1.43	1.25	0.27	0.08	17
11.0	1.42	1.33	0.23	0.12	15
11.1	1.31	1.27	0.22	0.14	18
11.2	1.35	1.19	0.37	0.14	14
11.3	1.47	1.18	0.43	0.11	14
11.4	1.48	1.22	0.43	0.16	18
11.5	1.35	1.35	0.15	0.15	13
11.6	1.34	1.34	0.16	0.16	12
11.7	1.38	1.23	0.41	0.17	13
11.8	1.49	1.24	0.40	0.16	12
11.9	1.54	1.26	0.34	0.13	11
12.0	1.30	1.26	0.23	0.15	12
12.2	1.51	1.26	0.44	0.19	14
12.4	1.46	1.31	0.44	0.24	10
12.6	1.50	1.23	0.49	0.20	10
12.8	1.41	1.31	0.38	0.21	10
13.0	1.40	1.37	0.25	0.21	19
13.2	1.54	1.31	0.43	0.23	10
13.4	1.57	1.35	0.43	0.21	9.1
13.6	1.42	1.41	0.27	0.27	10
13.8	1.45	1.37	0.44	0.32	9.0
14.0	1.57	1.37	0.52	0.29	9.0
14.2	1.58	1.38	0.53	0.30	9.0
14.4	1.62	1.39	0.56	0.31	9.2
14.6	1.56	1.40	0.55	0.36	9.0
14.8	1.56	1.41	0.55	0.37	9.0
15.0	1.43	1.28	0.53	0.30	10
15.2	1.45	1.33	0.49	0.32	10
15.4	1.43	1.31	0.50	0.31	10
15.6	1.46	1.36	0.52	0.38	8.9
15.8	1.55	1.36	0.62	0.40	8.7
16.0	1.58	1.41	0.62	0.42	8.9
16.2	1.61	1.42	0.66	0.44	8.9
16.4	1.63	1.45	0.67	0.46	8.8
16.6	1.63	1.44	0.68	0.47	9.1
16.8	1.74	1.32	0.84	0.48	10
17.0	1.76	1.35	0.87	0.52	9.0
17.1	1.77	1.37	0.86	0.53	8.9
17.2	1.74	1.34	0.87	0.52	9.1
17.3	1.82	1.39	0.84	0.53	9.0
17.4	1.50	1.37	0.63	0.45	10
17.5	1.82	1.40	0.85	0.54	9.1
17.6	1.87	1.46	0.85	0.59	10
17.7	1.73	1.58	0.64	0.52	9.1
17.8	1.83	1.40	0.91	0.59	9.1
17.9	1.84	1.41	0.87	0.58	9.3
18.0	1.49	1.38	0.55	0.40	26
18.1	1.53	1.39	0.65	0.46	11
18.2	1.54	1.41	0.84	0.70	9.4
18.3	1.70	1.43	0.88	0.69	9.5
18.4	1.51	1.40	0.48	0.33	51
18.5	1.55	1.41	0.68	0.50	11
18.6	1.51	1.41	0.57	0.42	22
18.7	1.55	1.41	0.66	0.48	10
18.8	1.57	1.42	0.69	0.50	11
18.9	1.63	1.47	0.76	0.56	11
19.0	1.63	1.44	0.80	0.57	11
19.2	1.59	1.44	0.72	0.53	10
19.4	1.56	1.44	0.70	0.54	10
19.6	1.63	1.45	0.79	0.57	11
19.8	1.61	1.43	0.79	0.58	10
20.0	1.46	1.46	0.62	0.61	13
20.5	1.64	1.46	0.79	0.56	13
21.0	1.50	1.49	0.71	0.70	10
21.5	1.61	1.45	0.80	0.59	14
22.0	1.52	1.36	0.92	0.72	11
22.5	1.49	1.43	0.68	0.58	11
23.0	1.63	1.46	0.90	0.68	11
23.5	1.92	1.58	1.19	0.87	12
24.0	2.07	1.64	1.34	0.98	12
24.5	2.20	1.67	1.47	1.07	13
25.0	2.17	1.59	1.43	1.02	19
25.5	1.87	1.62	1.08	0.82	14
26.0	1.74	1.53	1.15	0.90	15
26.5	1.80	1.54	1.19	0.90	16
27.0	1.73	1.52	1.12	0.89	18
27.5	1.59	1.46	1.14	0.96	16
28.0	1.60	1.46	1.06	0.88	21
28.5	1.62	1.43	1.22	0.98	19
29.0	1.72	1.49	1.26	1.01	15
29.5	1.70	1.45	1.29	1.00	15
30.0	1.75	1.50	1.24	0.97	20
30.5	1.77	1.51	1.36	1.09	14
31.0	1.84	1.54	1.46	1.15	15
31.5	1.93	1.58	1.56	1.24	18
32.0	1.94	1.57	1.60	1.27	15
32.5	1.98	1.59	1.65	1.30	18
33.0	2.08	1.63	1.77	1.41	16
33.5	2.12	1.64	1.79	1.42	24
34.0	2.12	1.64	1.85	1.48	16
34.5	2.19	1.65	1.91	1.52	19
35.0	2.24	1.66	1.95	1.56	21
36.0	2.33	1.80	2.06	1.73	17
37.0	2.25	1.82	2.20	1.96	18
38.0	2.23	1.66	1.87	1.49	59
39.0	2.24	1.78	1.76	1.44	739
40.0	2.16	1.88	2.60	2.50	23
41.0	2.27	1.85	2.31	2.10	50
42.0	2.24	1.93	2.49	2.35	30
43.0	1.97	1.75	2.82	2.79	26
44.0	1.64	1.64	2.86	2.86	23
45.0	2.20	1.91	2.30	2.18	896
50.0	2.34	1.82	2.08	1.80	2,020
55.0	1.91	1.91	2.82	2.82	2,048
60.0	1.91	1.91	3.21	3.21	150
65.0	1.97	1.95	3.16	3.15	1,830
70.0	2.18	1.96	3.87	3.72	184
75.0	2.15	2.04	3.71	3.63	2,305
80.0	2.26	2.14	3.88	3.81	2,334
85.0	2.42	2.03	4.17	4.05	2,526
90.0	2.40	1.54	4.11	3.92	2,648
95.0	2.53	2.04	4.26	4.11	1,214
100.0	2.02	1.44	3.34	2.92	1.3

Table 2: Summary of Solar Metallicity Presupernova Model Data

mass ($M_\odot$)	$M_{\rm final}$ ($M_\odot$)	$M_{\rm S=4}$ ($M_\odot$)	Fe core ($M_\odot$)	$BE_{\rm Fe\ core}$ (B)	$BE_{\rm S=4}$ (B)	$R_{\rm eff}$ ($R_\odot$)	mass ($M_\odot$)	$M_{\rm final}$ ($M_\odot$)	$M_{\rm S=4}$ ($M_\odot$)	Fe core ($M_\odot$)	$BE_{\rm Fe\ core}$ (B)	$BE_{\rm S=4}$ (B)	$R_{\rm eff}$ ($R_\odot$)
10.0	9.70	1.35	1.30	0.19	0.11	458	27.0	15.21	1.74	1.52	1.08	0.83	1,449
11.0	10.67	1.37	1.31	0.23	0.19	558	28.0	15.17	1.54	1.48	1.09	1.03	1,466
12.0	10.91	1.53	1.36	0.30	0.17	618	29.0	14.17	1.64	1.47	1.05	0.85	1,477
13.0	11.40	1.55	1.40	0.46	0.28	709	30.0	13.88	1.73	1.50	1.08	0.84	1,489
14.0	12.01	1.70	1.51	0.44	0.28	759	31.0	13.63	1.70	1.48	1.12	0.86	1,446
15.0	12.79	1.81	1.48	0.53	0.32	803	32.0	13.41	1.78	1.52	1.22	0.94	1,362
16.0	13.59	1.50	1.37	0.51	0.34	839	33.0	13.24	1.84	1.55	1.30	1.01	1,296
17.0	14.12	1.54	1.40	0.57	0.39	883	35.0	13.66	1.97	1.63	1.47	1.16	WNL
18.0	14.82	1.89	1.49	0.70	0.37	942	40.0	15.34	2.34	1.82	1.93	1.61	WNL
19.0	15.48	1.64	1.45	0.68	0.45	990	45.0	13.02	2.27	1.79	1.76	1.44	WO
20.0	15.93	1.82	1.54	0.89	0.60	1,032	50.0	9.82	1.70	1.49	1.05	0.81	WO
21.0	16.16	1.46	1.46	0.48	0.47	1,085	55.0	9.38	1.65	1.47	1.03	0.82	WO
22.0	16.16	1.84	1.54	0.95	0.65	1,139	60.0	7.29	1.60	1.45	0.71	0.53	WO
23.0	16.37	2.12	1.73	1.18	0.86	1,207	70.0	6.41	1.72	1.50	0.82	0.56	WC
24.0	16.22	2.05	1.70	1.17	0.87	1,270	80.0	6.37	1.66	1.48	0.76	0.54	WC
25.0	15.84	1.90	1.59	1.16	0.86	1,329	100.0	6.04	1.81	1.54	0.81	0.58	WC
26.0	15.41	1.73	1.54	0.97	0.74	1,386	120.0	6.00	1.60	1.43	0.68	0.48	WC

Table 3: $Z = 0$ Baryonic Remnant Masses

Run	ZA	ZB	ZC	ZD	ZE	ZF	ZG	ZH	ZI	ZJ	ZP	ZV
Energy (B)	0.3	0.6	0.9	1.2	1.5	1.8	2.4	3.0	5.0	10.0	1.2	10.0
Piston	$S = 4$	$S = 4$	$S = 4$	$S = 4$	$S = 4$	$S = 4$	$S = 4$	$S = 4$	$S = 4$	$S = 4$	Ye core	Ye core
Initial Mass	Remnant Mass											
($M_\odot$)	($M_\odot$)	($M_\odot$)	($M_\odot$)	($M_\odot$)	($M_\odot$)	($M_\odot$)	($M_\odot$)	($M_\odot$)	($M_\odot$)	($M_\odot$)	($M_\odot$)	($M_\odot$)
10.0	1.37	1.28	1.28	1.28	1.28	1.28	1.28	1.28	1.27	1.27	1.28	1.27
10.2	1.39	1.38	1.38	1.38	1.38	1.38	1.38	1.38	1.38	1.38	1.18	1.18
10.4	1.60	1.33	1.32	1.32	1.32	1.32	1.32	1.32	1.32	1.32	1.20	1.18
10.5	1.53	1.43	1.42	1.42	1.41	1.41	1.41	1.41	1.41	1.41	1.20	1.20
10.6	1.44	1.41	1.41	1.40	1.40	1.40	1.40	1.40	1.40	1.40	1.20	1.20
10.7	1.55	1.43	1.42	1.42	1.41	1.41	1.41	1.41	1.41	1.41	1.20	1.19
10.8	1.60	1.49	1.36	1.35	1.34	1.34	1.34	1.34	1.34	1.34	1.18	1.17
10.9	1.59	1.46	1.45	1.44	1.43	1.43	1.43	1.43	1.43	1.43	1.27	1.25
11.0	1.64	1.57	1.47	1.44	1.43	1.43	1.43	1.43	1.43	1.43	1.35	1.33
11.1	1.96	1.40	1.32	1.31	1.31	1.31	1.31	1.31	1.31	1.31	1.28	1.27
11.2	1.71	1.60	1.39	1.36	1.36	1.35	1.35	1.35	1.35	1.35	1.23	1.19
11.3	1.76	1.51	1.49	1.48	1.47	1.47	1.47	1.47	1.47	1.47	1.26	1.18
11.4	2.03	1.74	1.53	1.50	1.49	1.49	1.49	1.48	1.48	1.48	1.27	1.22
11.5	1.80	1.64	1.40	1.36	1.36	1.36	1.35	1.35	1.35	1.35	1.36	1.35
11.6	1.89	1.67	1.41	1.36	1.35	1.35	1.35	1.34	1.34	1.34	1.36	1.34
11.7	1.93	1.72	1.52	1.42	1.39	1.39	1.38	1.38	1.38	1.38	1.54	1.23
11.8	2.03	1.78	1.57	1.53	1.50	1.50	1.50	1.49	1.49	1.49	1.54	1.24
11.9	2.03	1.67	1.56	1.54	1.54	1.54	1.54	1.54	1.53	1.53	1.46	1.26
12.0	2.02	1.63	1.32	1.31	1.31	1.31	1.30	1.30	1.30	1.30	1.32	1.26
12.2	2.43	2.01	1.64	1.54	1.52	1.51	1.51	1.51	1.51	1.51	1.72	1.26
12.4	2.36	2.03	1.87	1.62	1.50	1.47	1.46	1.46	1.46	1.46	1.78	1.31
12.6	2.46	2.04	1.72	1.55	1.53	1.51	1.50	1.50	1.50	1.50	1.82	1.23
12.8	2.52	2.11	1.74	1.44	1.42	1.41	1.41	1.41	1.41	1.41	1.60	1.31
13.0	2.57	2.09	1.60	1.41	1.40	1.40	1.40	1.40	1.40	1.40	1.45	1.37
13.2	2.77	2.23	1.89	1.60	1.57	1.55	1.54	1.54	1.54	1.54	1.93	1.31
13.4	2.84	2.23	1.66	1.59	1.58	1.57	1.57	1.57	1.57	1.57	1.93	1.35
13.6	2.94	2.38	2.08	1.62	1.45	1.43	1.42	1.42	1.42	1.42	1.66	1.41
13.8	3.10	2.52	2.29	1.90	1.57	1.47	1.45	1.45	1.45	1.45	2.05	1.37
14.0	3.24	2.60	2.30	1.83	1.66	1.61	1.58	1.57	1.57	1.57	2.19	1.37
14.2	3.32	2.67	2.35	1.89	1.68	1.63	1.59	1.59	1.58	1.58	2.24	1.38
14.4	3.51	2.87	2.52	1.98	1.73	1.67	1.63	1.63	1.62	1.62	2.37	1.39
14.6	3.65	2.94	2.69	2.36	1.84	1.62	1.56	1.56	1.56	1.56	2.48	1.40
14.8	3.75	2.98	2.71	2.41	1.91	1.65	1.57	1.57	1.56	1.56	2.51	1.41
15.0	3.82	3.00	2.41	1.65	1.47	1.44	1.44	1.43	1.43	1.43	2.07	1.28
15.2	4.04	3.13	2.61	1.78	1.50	1.46	1.45	1.45	1.45	1.45	2.08	1.33
15.4	3.96	3.05	2.55	1.79	1.50	1.45	1.44	1.43	1.43	1.43	2.17	1.31
15.6	4.30	3.30	2.85	2.15	1.69	1.52	1.47	1.46	1.46	1.46	2.39	1.36
15.8	4.37	3.40	2.99	2.58	1.90	1.68	1.57	1.56	1.55	1.55	2.73	1.36
16.0	4.59	3.56	3.19	2.88	2.17	1.68	1.59	1.58	1.58	1.58	2.91	1.41
16.2	4.77	3.63	3.25	3.02	2.61	1.90	1.62	1.61	1.61	1.61	3.02	1.42
16.4	4.94	3.79	3.41	3.16	2.75	1.95	1.64	1.63	1.63	1.63	3.15	1.45
16.6	5.08	3.99	3.57	3.24	2.49	1.78	1.63	1.63	1.63	1.63	3.23	1.44
16.8	5.14	3.91	3.44	3.18	2.88	2.31	1.83	1.77	1.75	1.75	3.20	1.32
17.0	5.55	4.15	3.68	3.41	3.13	2.51	1.83	1.77	1.76	1.76	3.46	1.35
17.1	5.52	4.21	3.76	3.48	3.19	2.54	1.84	1.78	1.77	1.77	3.51	1.37
17.2	5.51	4.19	3.72	3.46	3.16	2.47	1.78	1.75	1.74	1.74	3.49	1.34
17.3	5.57	4.27	3.82	3.55	3.24	2.67	1.91	1.83	1.82	1.82	3.51	1.39
17.4	5.49	4.08	3.60	3.25	2.17	1.52	1.50	1.50	1.50	1.50	3.22	1.37
17.5	5.76	4.40	3.92	3.62	3.34	2.71	1.91	1.84	1.82	1.82	3.63	1.40
17.6	6.04	4.66	4.19	3.77	3.28	2.34	1.92	1.88	1.87	1.87	3.78	1.46
17.7	5.83	4.47	3.97	3.59	3.01	2.04	1.77	1.74	1.73	1.73	3.56	1.58
17.8	6.05	4.62	4.14	3.84	3.46	2.79	1.91	1.84	1.83	1.83	3.86	1.40
17.9	6.06	4.58	4.07	3.78	3.45	2.90	1.94	1.85	1.84	1.84	3.77	1.42
18.0	5.71	4.30	3.69	2.09	1.52	1.50	1.49	1.49	1.49	1.49	3.02	1.38
18.1	6.08	4.33	3.79	3.23	1.73	1.54	1.53	1.53	1.53	1.52	3.20	1.39
18.2	6.59	4.77	4.13	3.77	3.23	2.67	1.61	1.56	1.54	1.54	3.82	1.41
18.3	6.61	4.86	4.29	3.90	3.48	2.88	1.80	1.73	1.71	1.70	3.97	1.43
18.4	5.85	4.25	1.56	1.51	1.51	1.51	1.51	1.51	1.51	1.51	1.91	1.40
18.5	6.45	4.59	3.99	3.41	1.97	1.57	1.55	1.55	1.55	1.55	3.43	1.42

(continued on next page)

Table 3: $Z = 0$ Baryonic Remnant Masses (continued)

Run	ZA	ZB	ZC	ZD	ZE	ZF	ZG	ZH	ZI	ZJ	ZP	ZV
Energy (B)	0.3	0.6	0.9	1.2	1.5	1.8	2.4	3.0	5.0	10.0	1.2	10.0
Piston	$S = 4$	$S = 4$	$S = 4$	$S = 4$	$S = 4$	$S = 4$	$S = 4$	$S = 4$	$S = 4$	$S = 4$	Ye core	Ye core
Initial Mass	Remnant Mass											
($M_\odot$)	($M_\odot$)	($M_\odot$)	($M_\odot$)	($M_\odot$)	($M_\odot$)	($M_\odot$)	($M_\odot$)	($M_\odot$)	($M_\odot$)	($M_\odot$)	($M_\odot$)	($M_\odot$)
18.6	6.25	4.57	3.93	2.54	1.55	1.52	1.51	1.51	1.51	1.51	3.24	1.41
18.7	6.58	4.76	4.17	3.64	1.69	1.56	1.55	1.55	1.55	1.55	3.63	1.42
18.8	6.66	4.71	4.06	3.45	2.10	1.59	1.57	1.57	1.57	1.57	3.49	1.42
18.9	6.97	5.13	4.46	3.74	1.93	1.65	1.63	1.63	1.63	1.63	3.80	1.47
19.0	6.99	5.16	4.43	3.38	1.84	1.65	1.63	1.63	1.63	1.63	3.58	1.44
19.2	7.08	5.03	4.37	3.77	2.51	1.61	1.59	1.59	1.59	1.59	3.81	1.44
19.4	7.25	5.09	4.38	3.79	2.73	1.61	1.57	1.56	1.56	1.56	3.84	1.44
19.6	7.40	5.25	4.56	4.02	3.12	1.69	1.64	1.63	1.63	1.63	4.08	1.45
19.8	7.66	5.49	4.72	3.79	1.99	1.63	1.61	1.61	1.61	1.61	3.97	1.43
20.0	7.77	5.37	4.37	2.43	1.70	1.50	1.47	1.47	1.46	1.46	2.49	1.46
20.5	7.75	5.47	4.67	3.57	1.83	1.67	1.65	1.65	1.64	1.64	3.80	1.46
21.0	9.14	6.36	5.45	4.21	1.90	1.53	1.50	1.50	1.50	1.50	4.30	1.49
21.5	7.88	5.92	5.05	3.30	1.66	1.63	1.61	1.61	1.61	1.61	3.61	1.45
22.0	9.92	6.93	5.87	3.71	1.60	1.53	1.52	1.52	1.52	1.52	4.52	1.36
22.5	9.81	6.96	5.68	2.82	1.55	1.50	1.50	1.49	1.49	1.49	3.32	1.43
23.0	10.49	7.36	6.26	4.51	1.94	1.66	1.64	1.64	1.64	1.64	5.00	1.46
23.5	11.42	8.10	6.86	5.78	3.11	2.18	1.95	1.93	1.92	1.92	6.22	1.59
24.0	12.32	8.54	7.23	6.47	5.11	3.02	2.18	2.10	2.08	2.07	6.67	1.65
24.5	12.64	8.91	7.47	6.66	4.70	2.60	2.30	2.23	2.21	2.20	6.87	1.68
25.0	10.19	7.96	7.13	4.16	2.57	2.35	2.21	2.19	2.17	2.17	5.96	1.60
25.5	13.48	9.41	7.68	2.01	1.90	1.88	1.87	1.87	1.87	1.87	3.00	1.62
26.0	14.22	9.94	8.14	2.08	1.77	1.75	1.74	1.74	1.74	1.74	3.91	1.53
26.5	14.41	9.97	8.29	6.41	1.88	1.82	1.81	1.81	1.80	1.80	7.23	1.55
27.0	12.03	8.92	7.26	1.96	1.77	1.74	1.73	1.73	1.73	1.73	2.30	1.52
27.5	15.71	11.13	9.15	3.16	1.63	1.61	1.60	1.59	1.59	1.59	6.89	1.46
28.0	12.90	9.51	7.76	1.92	1.63	1.61	1.60	1.60	1.60	1.60	2.19	1.46
28.5	16.36	11.72	9.42	2.54	1.68	1.64	1.63	1.63	1.63	1.62	7.50	1.43
29.0	17.29	12.15	10.16	8.23	2.21	1.83	1.74	1.73	1.72	1.72	8.95	1.49
29.5	17.77	12.75	10.25	7.56	1.99	1.76	1.71	1.71	1.70	1.70	8.83	1.46
30.0	15.40	11.12	9.55	2.73	1.97	1.83	1.77	1.76	1.75	1.75	4.56	1.51
30.5	18.91	13.70	11.16	9.74	3.15	1.98	1.79	1.78	1.77	1.77	9.96	1.52
31.0	19.37	14.10	11.47	10.06	3.89	2.16	1.89	1.86	1.85	1.84	10.17	1.54
31.5	19.53	14.48	12.04	10.29	2.62	2.14	1.98	1.95	1.94	1.94	10.74	1.59
32.0	20.62	15.25	12.45	11.04	7.66	2.53	2.02	1.96	1.95	1.94	11.20	1.58
32.5	21.01	15.41	12.73	11.32	5.49	2.42	2.05	2.01	1.99	1.98	11.48	1.61
33.0	21.70	16.32	13.41	11.95	8.60	2.79	2.20	2.11	2.08	2.08	12.17	1.65
33.5	21.17	16.19	13.43	11.82	3.59	2.53	2.22	2.15	2.13	2.12	11.96	1.66
34.0	23.15	17.25	14.18	12.46	11.09	3.74	2.33	2.18	2.13	2.12	12.66	1.66
34.5	23.41	17.73	14.65	12.88	11.29	3.28	2.38	2.25	2.21	2.20	13.06	1.67
35.0	23.51	18.05	14.84	13.08	11.12	3.17	2.43	2.29	2.25	2.24	13.37	1.68
36.0	26.27	19.60	16.27	14.12	12.95	10.04	2.86	2.47	2.35	2.33	14.43	1.82
37.0	27.91	20.61	17.19	14.85	13.59	11.58	3.02	2.58	2.31	2.26	15.09	1.85
38.0	20.96	16.24	14.08	11.43	3.99	3.16	2.54	2.32	2.24	2.23	11.95	1.68
39.0	14.27	11.54	8.06	6.24	4.61	3.52	2.71	2.40	2.25	2.24	6.75	1.79
40.0	32.12	24.05	20.64	18.16	16.48	15.29	6.15	3.38	2.40	2.19	18.32	1.92
41.0	25.86	20.31	17.51	15.90	13.73	5.41	3.73	3.09	2.44	2.29	16.02	1.88
42.0	31.18	23.52	20.18	18.14	16.53	15.01	4.04	3.35	2.48	2.27	18.15	1.96
43.0	34.27	26.63	23.09	20.69	18.85	17.56	12.69	4.25	2.45	2.00	20.85	1.79
44.0	35.94	28.69	24.78	22.23	20.40	18.98	16.07	5.23	2.60	1.66	22.22	1.66
45.0	16.94	12.90	11.14	9.08	7.47	6.31	4.46	3.57	2.52	2.23	9.41	1.95
50.0	15.46	13.94	12.69	11.67	10.66	9.20	5.85	3.64	2.47	2.36	11.89	1.86
55.0	18.14	16.46	14.50	12.60	10.95	9.50	7.21	5.73	3.39	1.96	12.59	1.96
60.0	43.32	34.58	29.61	27.46	25.88	24.62	11.75	9.35	4.56	1.93	27.45	1.93
65.0	24.00	22.80	21.57	19.95	18.22	16.44	13.20	10.50	4.89	1.99	20.01	1.99
70.0	52.95	45.53	38.23	35.35	33.35	31.71	29.03	14.53	6.57	2.21	35.21	2.08
75.0	28.07	26.96	25.96	24.63	23.25	21.55	18.42	15.60	8.88	2.25	24.62	2.20
80.0	29.61	29.41	27.99	27.09	25.99	24.49	21.39	18.52	11.14	2.40	27.06	2.32
85.0	27.68	27.69	27.62	27.23	26.17	24.93	22.41	19.93	13.28	5.15	27.32	4.44
90.0	26.83	26.86	26.77	26.83	26.77	26.25	24.41	21.92	15.26	7.02	27.41	6.90
95.0	29.06	29.04	28.30	26.87	25.48	24.10	21.23	18.49	12.10	3.24	26.32	3.30
100.0	40.01	38.34	36.95	35.70	34.12	31.79	25.08	13.35	2.12	2.03	35.78	1.53

Table 4: $Z =$ solar Baryonic Remnant Masses

Run	SA	SB	SC	SD
Energy (B)	1.2	2.4	1.2	2.4
Piston	$S = 4$	$S = 4$	Fe core	Fe core
Initial Mass	Remnant Mass			
(M$_\odot$)	(M$_\odot$)	(M$_\odot$)	(M$_\odot$)	(M$_\odot$)
12.0	1.53	1.52	1.37	1.37
13.0	1.56	1.55	1.48	1.41
14.0	1.71	1.70	1.57	1.52
15.0	1.84	1.83	1.58	1.49
16.0	2.09	1.50	1.46	1.39
17.0	1.54	1.54	1.52	1.42
18.0	1.90	1.89	1.89	1.54
19.0	1.66	1.64	1.71	1.49
20.0	1.86	1.82	1.96	1.62
21.0	1.48	1.46	1.48	1.46
22.0	1.93	1.84	2.13	1.67
23.0	2.36	2.14	2.75	1.95
24.0	2.29	2.06	2.64	1.89
25.0	2.09	1.91	2.43	1.81
26.0	1.75	1.74	1.82	1.61
27.0	1.82	1.75	1.96	1.62
28.0	2.39	1.59	2.49	1.59
29.0	1.76	1.64	2.02	1.57
30.0	1.95	1.74	2.23	1.68
31.0	1.96	1.71	2.33	1.67
32.0	2.27	1.79	2.62	1.79
33.0	2.52	1.85	2.89	1.87
35.0	3.21	2.02	3.85	2.13
40.0	5.60	2.73	6.72	3.15
45.0	3.93	2.45	5.03	2.70
50.0	1.88	1.71	2.22	1.64
55.0	1.76	1.66	2.05	1.57
60.0	1.64	1.60	1.71	1.51
70.0	2.06	1.74	2.18	1.72
80.0	2.03	1.67	2.05	1.65
100.0	2.08	1.85	2.16	1.75

Table 5: Remnant Mass Averages and Distributions

Z	piston	$E_{\rm exp}$ (B)	BH (%)	$\log(M_{\rm BH})$ ($M_\odot$)	BH mass ($M_\odot$)	NS mass ($M_\odot$)
assume maximum neutron star gravitational mass of 1.7 $M_\odot$						
solar	S=4	1.2	23.96	0.41 ± 0.14	2.71 ± 1.02	1.41 ± 0.15
solar	S=4	2.4	10.63	0.35 ± 0.05	2.25 ± 0.25	1.40 ± 0.13
solar	Fe	1.2	25.48	0.45 ± 0.16	3.06 ± 1.33	1.34 ± 0.14
solar	Fe	2.4	7.15	0.41 ± 0.07	2.57 ± 0.38	1.33 ± 0.12
0	S=4	0.3	75.09	0.86 ± 0.38	10.66 ± 9.64	1.39 ± 0.15
0	S=4	0.6	70.39	0.79 ± 0.36	8.86 ± 8.26	1.32 ± 0.14
0	S=4	0.9	60.25	0.80 ± 0.33	8.66 ± 7.54	1.33 ± 0.14
0	S=4	1.2	52.63	0.75 ± 0.35	7.93 ± 7.47	1.33 ± 0.14
0	S=4	1.5	34.85	0.76 ± 0.38	8.60 ± 8.04	1.36 ± 0.15
0	S=4	1.8	26.31	0.76 ± 0.40	8.80 ± 8.24	1.35 ± 0.13
0	S=4	2.4	19.59	0.72 ± 0.38	7.88 ± 7.39	1.35 ± 0.13
0	S=4	3.0	19.36	0.63 ± 0.33	5.91 ± 5.51	1.35 ± 0.12
0	S=4	5.0	18.89	0.50 ± 0.24	3.85 ± 3.10	1.35 ± 0.12
0	S=4	10.0	17.55	0.36 ± 0.10	2.37 ± 0.79	1.36 ± 0.13
0	Fe	1.2	59.00	0.74 ± 0.34	7.63 ± 7.18	1.28 ± 0.19
0	Fe	10.0	5.23	0.39 ± 0.16	2.67 ± 1.26	1.27 ± 0.15
assume maximum neutron star gravitational mass of 2.0 $M_\odot$						
solar	S=4	1.2	8.59	0.56 ± 0.12	3.80 ± 1.02	1.47 ± 0.21
solar	S=4	2.4	3.72	0.41 ± 0.02	2.56 ± 0.11	1.43 ± 0.17
solar	Fe	1.2	14.53	0.55 ± 0.15	3.76 ± 1.40	1.40 ± 0.22
solar	Fe	2.4	4.77	0.45 ± 0.04	2.80 ± 0.23	1.34 ± 0.15
0	S=4	0.3	70.44	0.90 ± 0.36	11.22 ± 9.68	1.45 ± 0.20
0	S=4	0.6	60.26	0.87 ± 0.33	10.00 ± 8.41	1.45 ± 0.25
0	S=4	0.9	56.26	0.83 ± 0.32	9.11 ± 7.60	1.38 ± 0.22
0	S=4	1.2	47.74	0.79 ± 0.33	8.52 ± 7.59	1.37 ± 0.20
0	S=4	1.5	30.18	0.83 ± 0.36	9.61 ± 8.19	1.39 ± 0.18
0	S=4	1.8	21.93	0.84 ± 0.38	10.14 ± 8.41	1.38 ± 0.17
0	S=4	2.4	14.16	0.88 ± 0.34	10.08 ± 7.62	1.39 ± 0.17
0	S=4	3.0	13.15	0.77 ± 0.31	7.70 ± 5.89	1.39 ± 0.17
0	S=4	5.0	10.85	0.62 ± 0.26	5.11 ± 3.62	1.40 ± 0.19
0	S=4	10.0	1.79	0.59 ± 0.16	4.16 ± 1.55	1.44 ± 0.22
0	Fe	1.2	51.83	0.79 ± 0.32	8.39 ± 7.35	1.37 ± 0.27
0	Fe	10.0	1.38	0.62 ± 0.14	4.41 ± 1.34	1.29 ± 0.18

Table 6: Remnant Mass Averages and Distributions by Origin

range ($M_\odot$)	BH (%)	NS (%)	$\log(M_{\rm BH})$ ($M_\odot$)	BH mass ($M_\odot$)	NS mass ($M_\odot$)
Case: $Z =$ solar, $E = 1.2\,$B, piston at $S = 4$, $M_{\rm NS}^{\rm max} = 1.7\,{\rm M}_\odot$					
< 10	–	12.44	–	–	1.24 ± 0.00
$10 - 12$	–	20.00	–	–	1.27 ± 0.04
$12 - 15$	–	18.64	–	–	1.46 ± 0.08
$15 - 20$	3.52	13.54	0.30 ± 0.01	2.02 ± 0.04	1.56 ± 0.08
$20 - 25$	4.93	4.42	0.35 ± 0.02	2.22 ± 0.11	1.50 ± 0.10
$25 - 40$	8.98	3.52	0.44 ± 0.14	2.93 ± 1.06	1.61 ± 0.04
> 40	6.53	3.48	0.46 ± 0.17	3.14 ± 1.25	1.57 ± 0.06
total	23.96	76.04	0.41 ± 0.14	2.71 ± 1.02	1.41 ± 0.15
Case: $Z =$ solar, $E = 1.2\,$B, piston at $S = 4$, $M_{\rm NS}^{\rm max} = 2.0\,{\rm M}_\odot$					
< 10	–	12.44	–	–	1.24 ± 0.00
$10 - 12$	–	20.00	–	–	1.27 ± 0.04
$12 - 15$	–	18.64	–	–	1.46 ± 0.08
$15 - 20$	–	17.06	–	–	1.60 ± 0.11
$20 - 25$	0.39	8.96	0.37 ± 0.00	2.36 ± 0.01	1.70 ± 0.22
$25 - 40$	4.86	7.63	0.55 ± 0.12	3.64 ± 0.98	1.72 ± 0.12
> 40	3.34	6.67	0.61 ± 0.10	4.18 ± 0.92	1.67 ± 0.12
total	8.59	91.41	0.56 ± 0.12	3.80 ± 1.02	1.47 ± 0.21
Case: $Z = 0$, $E = 1.2\,$B, piston at $S = 4$, $M_{\rm NS}^{\rm max} = 1.7\,{\rm M}_\odot$					
< 10	–	6.98	–	–	1.16 ± 0.00
$10 - 12$	–	21.24	–	–	1.26 ± 0.05
$12 - 15$	3.20	16.60	0.34 ± 0.03	2.22 ± 0.16	1.44 ± 0.13
$15 - 20$	15.62	2.50	0.50 ± 0.07	3.23 ± 0.50	1.56 ± 0.05
$20 - 25$	9.94	–	0.62 ± 0.12	4.28 ± 1.21	–
$25 - 40$	13.24	0.04	0.81 ± 0.30	7.95 ± 4.42	1.69 ± 0.00
> 40	10.63	–	1.27 ± 0.17	19.91 ± 7.18	–
total	52.63	47.37	0.75 ± 0.35	7.93 ± 7.47	1.33 ± 0.14
Case: $Z = 0$, $E = 1.2\,$B, piston at $S = 4$, $M_{\rm NS}^{\rm max} = 2.0\,{\rm M}_\odot$					
< 10	–	6.98	–	–	1.16 ± 0.00
$10 - 12$	–	21.24	–	–	1.26 ± 0.05
$12 - 15$	1.19	18.61	0.38 ± 0.00	2.38 ± 0.02	1.48 ± 0.17
$15 - 20$	14.43	3.70	0.52 ± 0.05	3.32 ± 0.40	1.65 ± 0.15
$20 - 25$	9.94	–	0.62 ± 0.12	4.28 ± 1.21	–
$25 - 40$	11.55	1.73	0.88 ± 0.25	8.81 ± 4.08	1.82 ± 0.08
> 40	10.63	–	1.27 ± 0.17	19.91 ± 7.18	–
total	47.74	52.26	0.79 ± 0.33	8.52 ± 7.59	1.37 ± 0.20

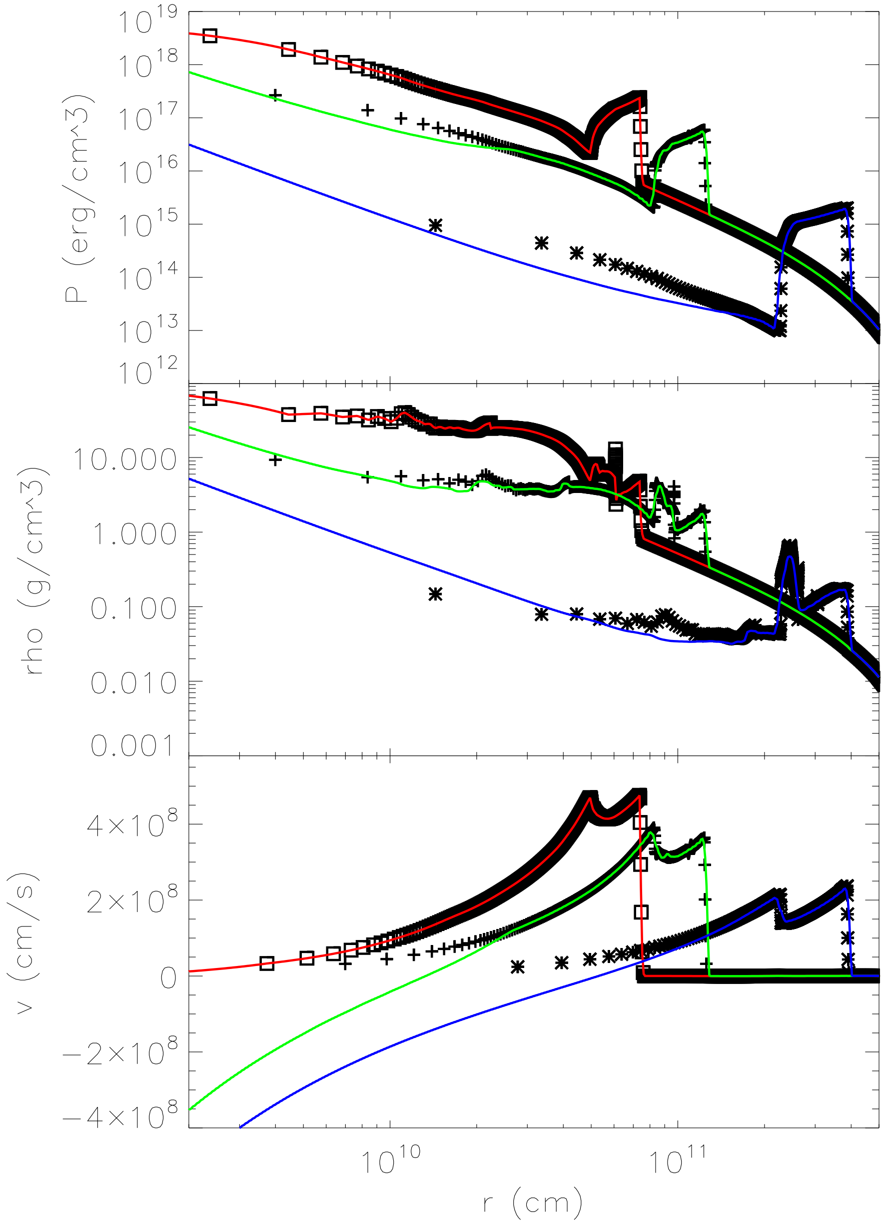

Fig. 1.— Pressure, density and velocity profiles at 100 (red lines and square symbols), 200 (green lines and plus symbols), and 1000 s (blue lines and star symbols) in Model Z25D calculated using Kepler (symbols) and Pangu (solid lines). The agreement is excellent except near the origin. Since Pangu uses a more realistic representation of the fallback at small radii, its results are preferred. The inner boundary in Pangu is inside the sonic radius at all times

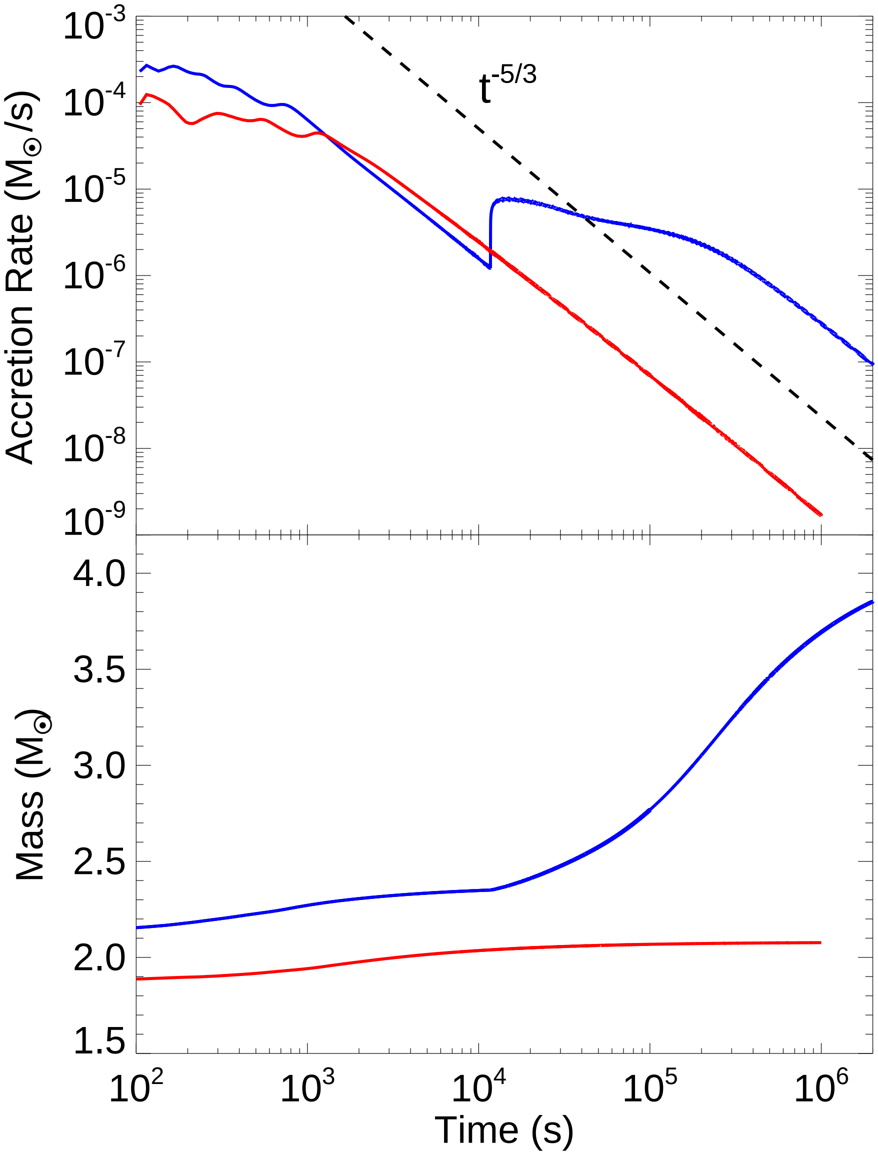

Fig. 2.— Accretion rates and central point mass for models Z25D (blue lines) and S25A (red lines). The dotted line shows the asymptotic accretion rate, $\sim t^{-5/3}$. Note the prominent appearance of the reverse shock at the core at about 10^4 s in Z25D. For model S25A the reverse shock has not arrived back at the origin at 10^6 s and, in fact, is still moving outwards in space. Its eventual arrival will have little consequence for the mass of the remnant. Note a period of about 1000 s during which the initial accretion rate is nearly constant.

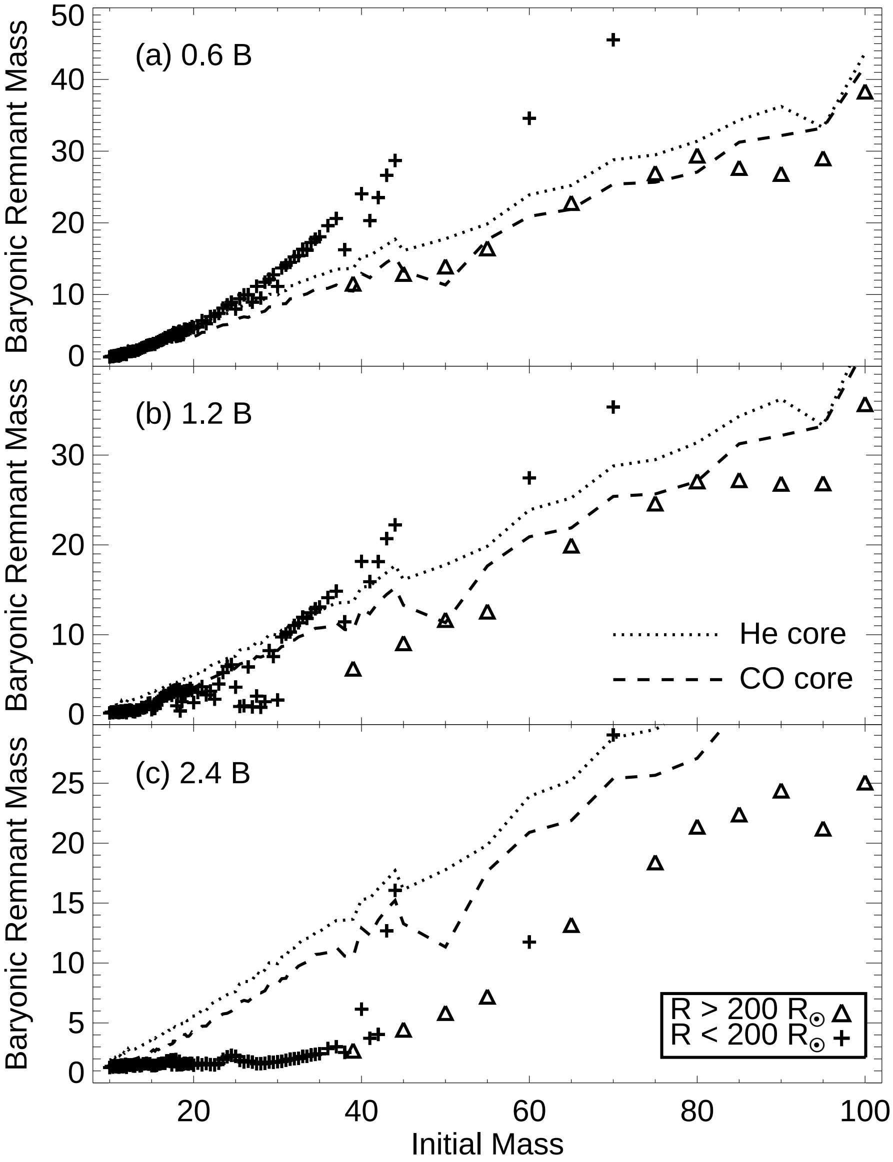

Fig. 3.— Comparison of baryonic remnant masses for (a) ZB, (b) ZD and (c) ZG models. The explosion energies are 0.6, 1.2 and 2.4 B, for models ZB, ZD and ZG, respectively. It is clear that there are two branches of remnant masses. The higher mass branch consists of compact stars with a radius less than 200 $R_\odot$, whereas the lower mass branch consists of red supergiants with a radius greater than 200 $R_\odot$. The positions of the He core (dotted lines) and CO core (dashed lines) in the initial models are also shown. Note that for the lower mass branch of ZB models the remnant mass is very close to the CO core mass.

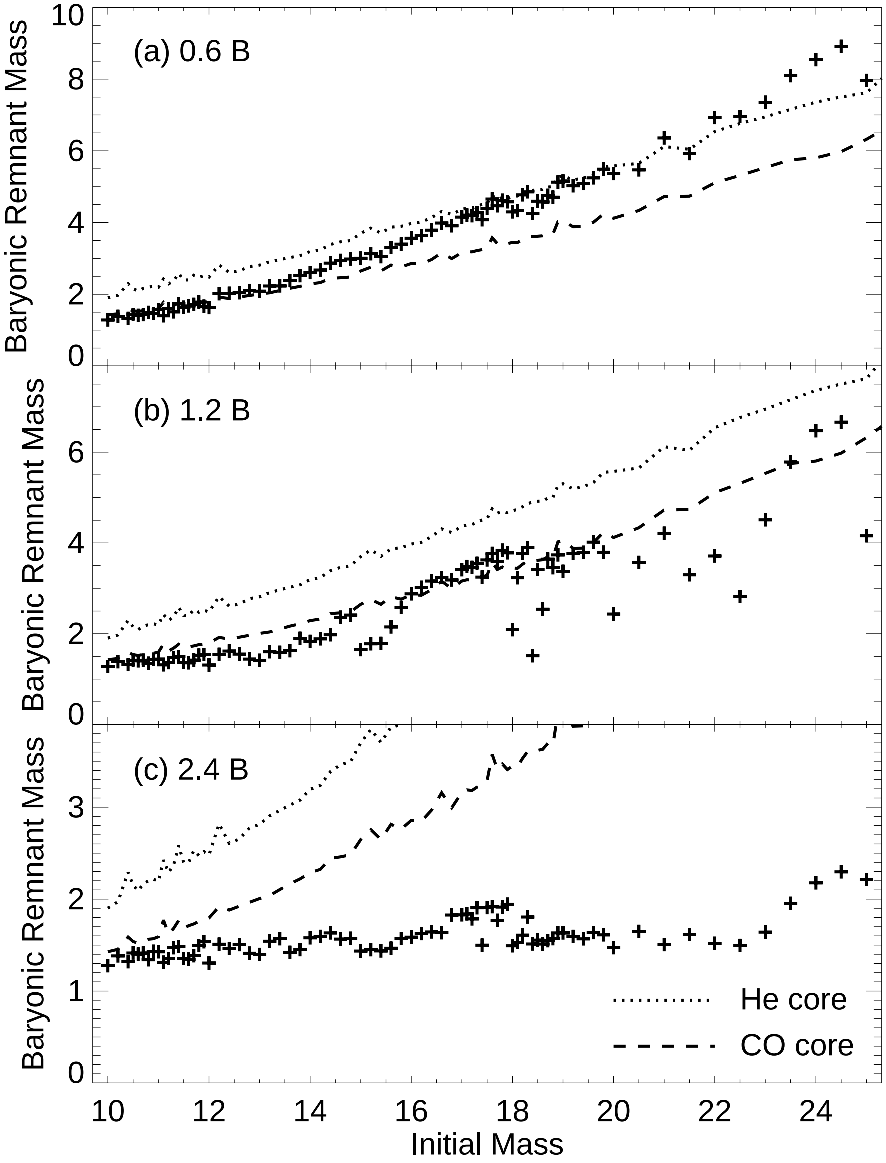

Fig. 4.— Baryonic remnant masses for (a) ZB, (b) ZD and (c) ZG models plotted on a finer scale for lower mass stars. The explosion energies are 0.6, 1.2 and 2.4 B, for models ZB, ZD and ZG, respectively. As we expected, ZG models make many neutron stars, whereas ZB models make many black holes.

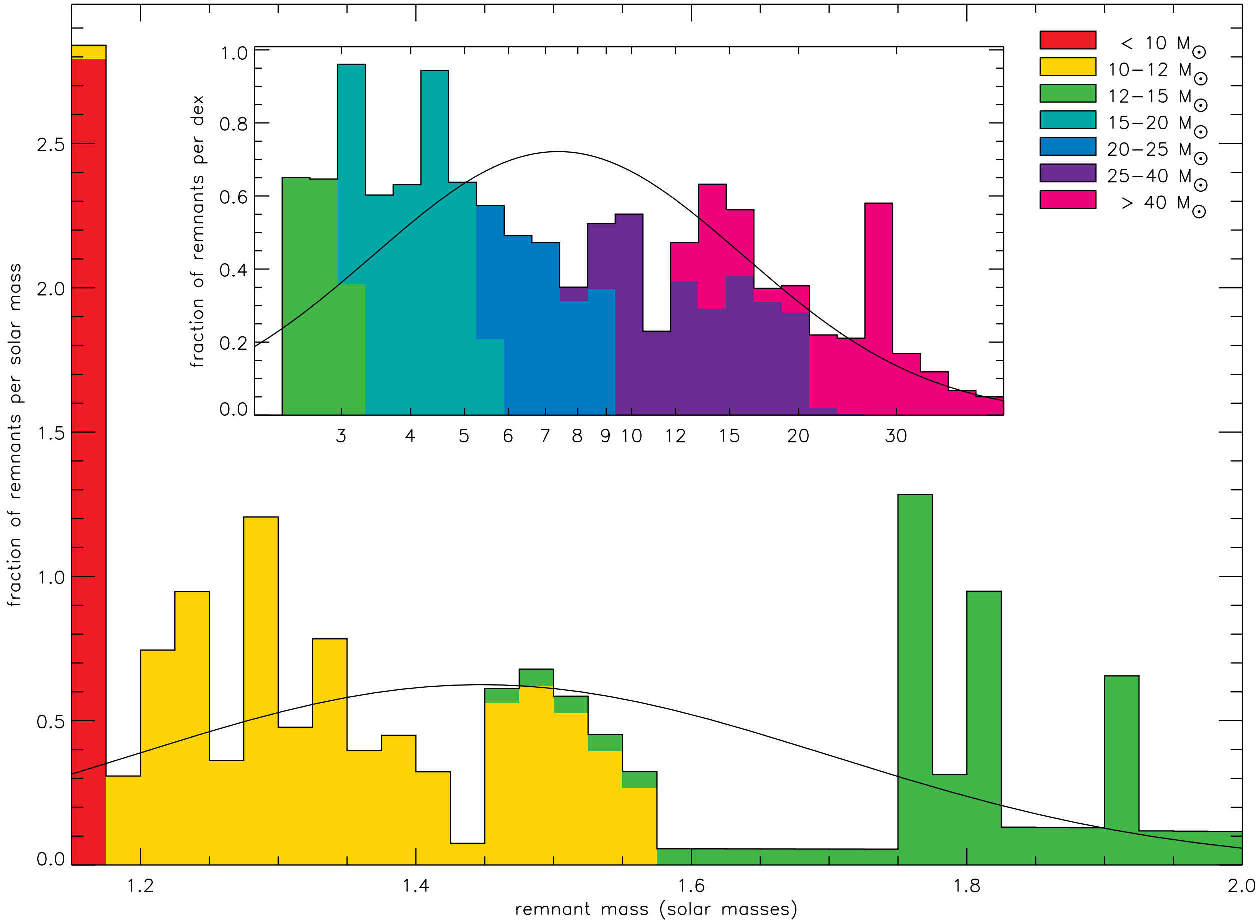

Fig. 5.— Distribution of remnant masses for 0.6 B explosions of metal-free stars with pistons located at the $S/N_A k = 4.0$ point, for an initial mass range of $9.5\,\mathrm{M}_\odot$ to $100\,\mathrm{M}_\odot$, and an assumed a maximum neutron stars mass of $2\,\mathrm{M}_\odot$. The main figure gives *gravitational* masses of neutron stars, the insert shows the *baryonic* masses of black holes. The color coding (cumulative) indicates the initial mass range of the progenitor stars. The curve is a Gaussian fit with the same average and variance as distribution for the neutron stars (main figure). For the insert the curve is a Gaussian fit to the logarithm of black hole masses (geometric fit). The normalization of the bins in the big plot is such that the sum over the bins times the bin width equals total fraction of neutron stars. For the inserts the normalization is not "per solar mass" but "per dex", i.e., the sum of bin height times bin width in dex equals the total fraction of black holes. The bin sizes are $0.025\,\mathrm{M}_\odot$ for the main figure and 0.05 dex for the insert.

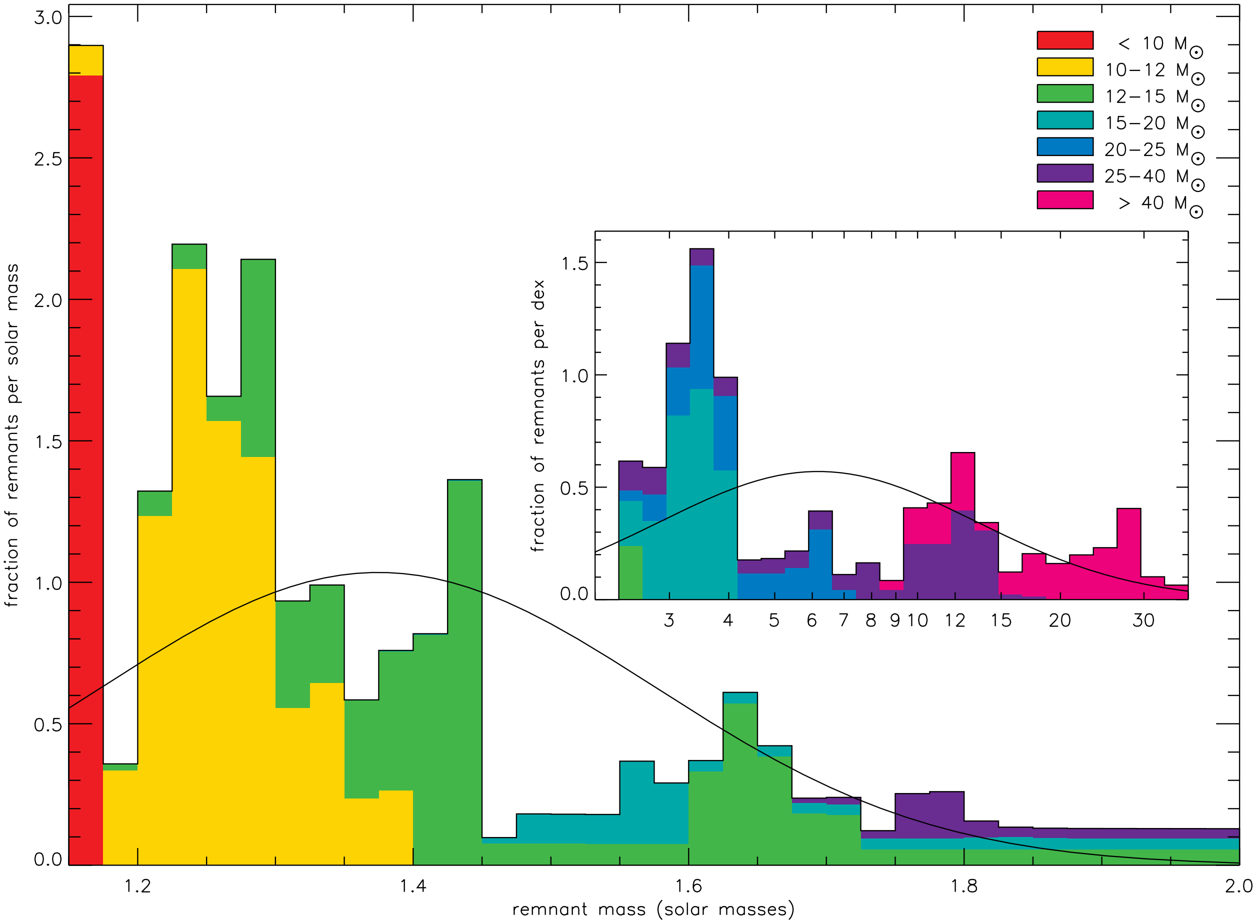

Fig. 6.— Distribution of remnant masses for 1.2 B explosions of metal-free stars with pistons located at the $S/N_A k = 4.0$ point, for an initial mass range of $9.5\,\mathrm{M}_\odot$ to $100\,\mathrm{M}_\odot$, and an assumed a maximum neutron stars mass of $2\,\mathrm{M}_\odot$. The main figure gives *gravitational* masses of neutron stars, the insert shows the *baryonic* masses of black holes. The color coding (cumulative) indicates the initial mass range of the progenitor stars. The curve is a Gaussian fit with the same average and variance as distribution for the neutron stars (main figure). For the insert the curve is a Gaussian fit to the logarithm of black hole masses (geometric fit). The normalization of the bins in the big plot is such that the sum over the bins times the bin width equals total fraction of neutron stars. For the inserts the normalization is not “per solar mass” but “per dex”, i.e., the sum of bin height times bin width in dex equals the total fraction of black holes. The bin sizes are $0.025\,\mathrm{M}_\odot$ for the main figure and 0.05 dex for the insert.

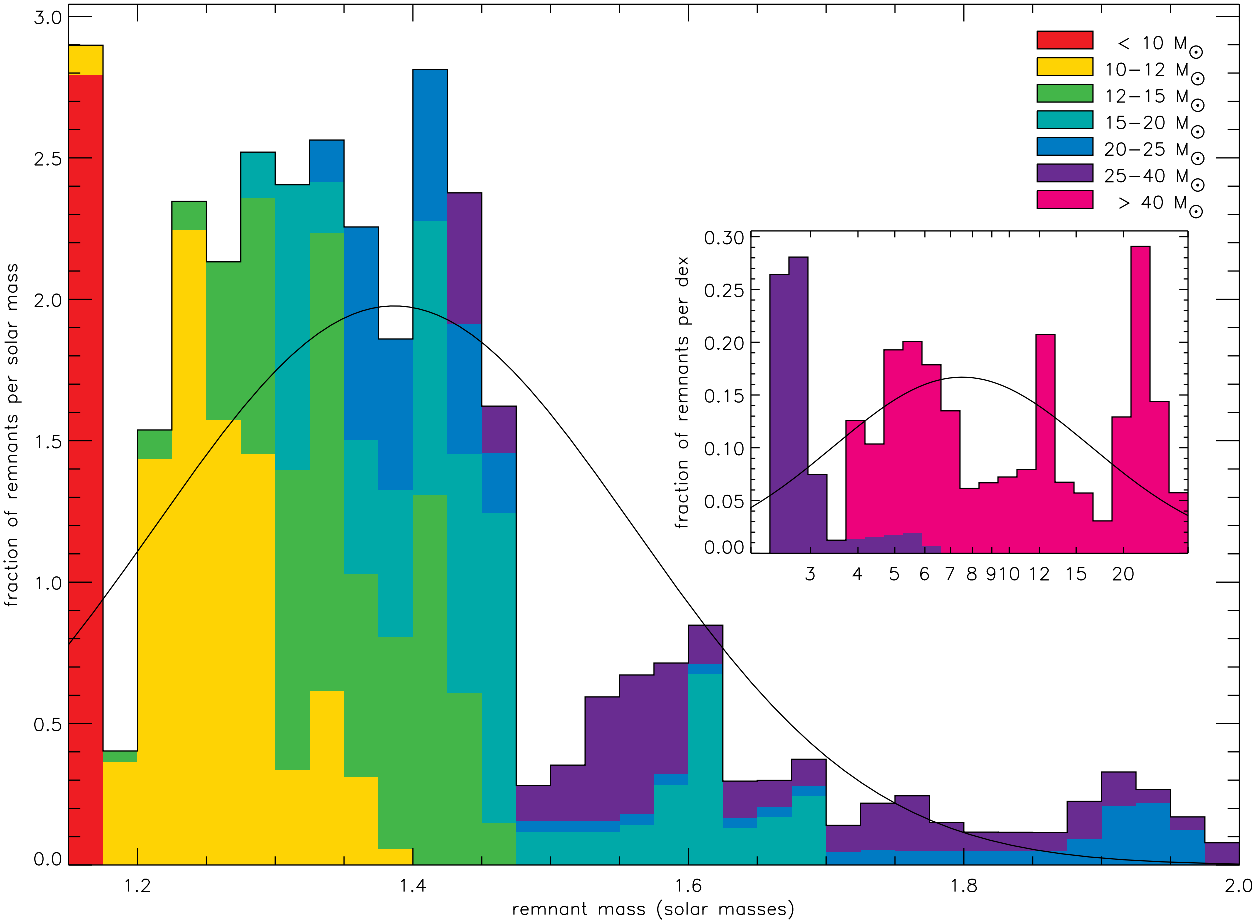

Fig. 7.— Distribution of remnant masses for 2.4 B explosions of metal-free stars with pistons located at the $S/N_A k = 4.0$ point, for an initial mass range of $9.5\,\mathrm{M}_\odot$ to $100\,\mathrm{M}_\odot$, and an assumed a maximum neutron stars mass of $2\,\mathrm{M}_\odot$. The main figure gives *gravitational* masses of neutron stars, the insert shows the *baryonic* masses of black holes. The color coding (cumulative) indicates the initial mass range of the progenitor stars. The curve is a Gaussian fit with the same average and variance as distribution for the neutron stars (main figure). For the insert the curve is a Gaussian fit to the logarithm of black hole masses (geometric fit). The normalization of the bins in the big plot is such that the sum over the bins times the bin width equals total fraction of neutron stars. For the inserts the normalization is not "per solar mass" but "per dex", i.e., the sum of bin height times bin width in dex equals the total fraction of black holes. The bin sizes are $0.025\,\mathrm{M}_\odot$ for the main figure and 0.05 dex for the insert.

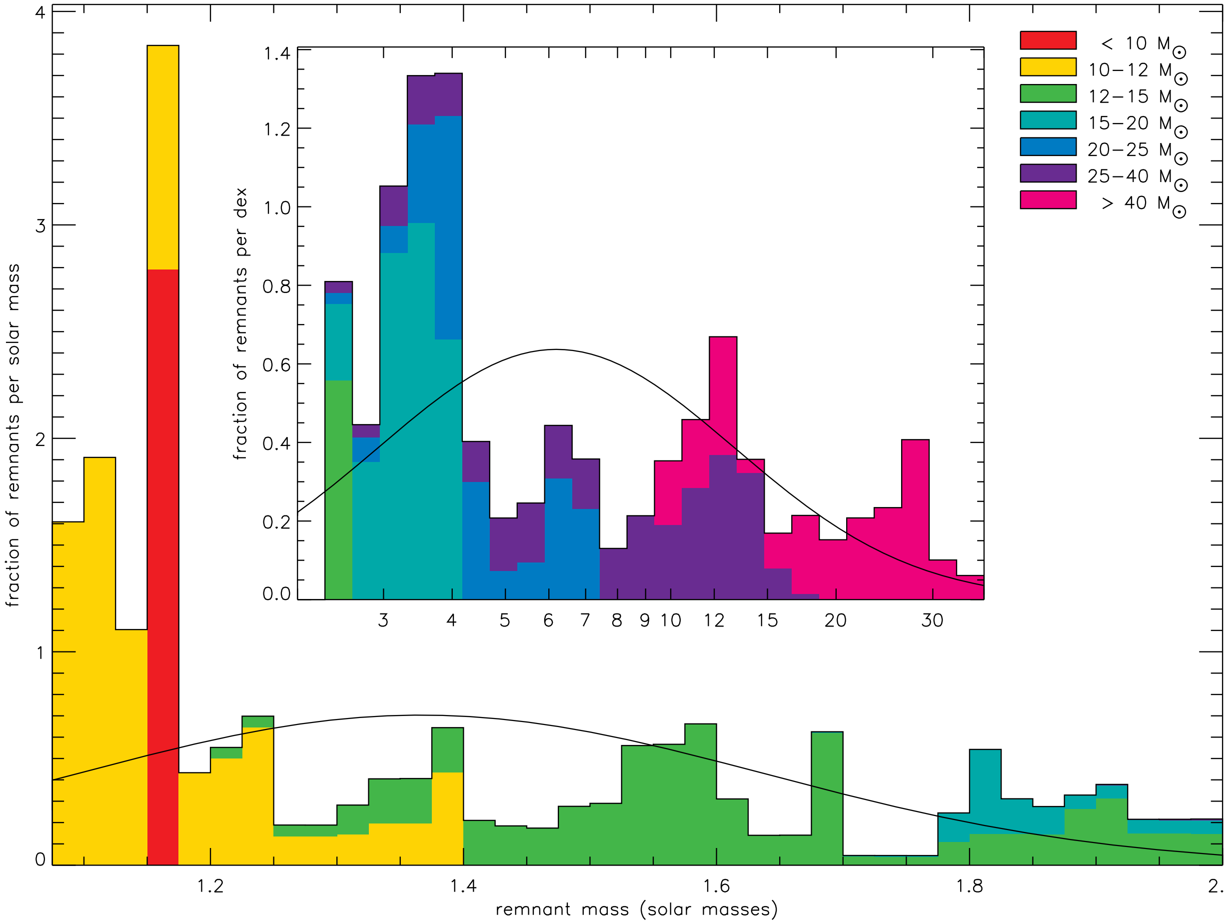

Fig. 8.— Distribution of remnant masses for 1.2 B explosions of metal-free stars with pistons located at the edge of the deleptonized core, for an initial mass range of 9.5 $M_{\odot}$ to 100 $M_{\odot}$, and an assumed a maximum neutron stars mass of 2 $M_{\odot}$. The main figure gives *gravitational* masses of neutron stars, the insert shows the *baryonic* masses of black holes. The color coding (cumulative) indicates the initial mass range of the progenitor stars. The curve is a Gaussian fit with the same average and variance as distribution for the neutron stars (main figure). For the insert the curve is a Gaussian fit to the logarithm of black hole masses (geometric fit). The normalization of the bins in the big plot is such that the sum over the bins times the bin width equals total fraction of neutron stars. For the inserts the normalization is not "per solar mass" but "per dex", i.e., the sum of bin height times bin width in dex equals the total fraction of black holes. The bin sizes are 0.025 $M_{\odot}$ for the main figure and 0.05 dex for the insert.

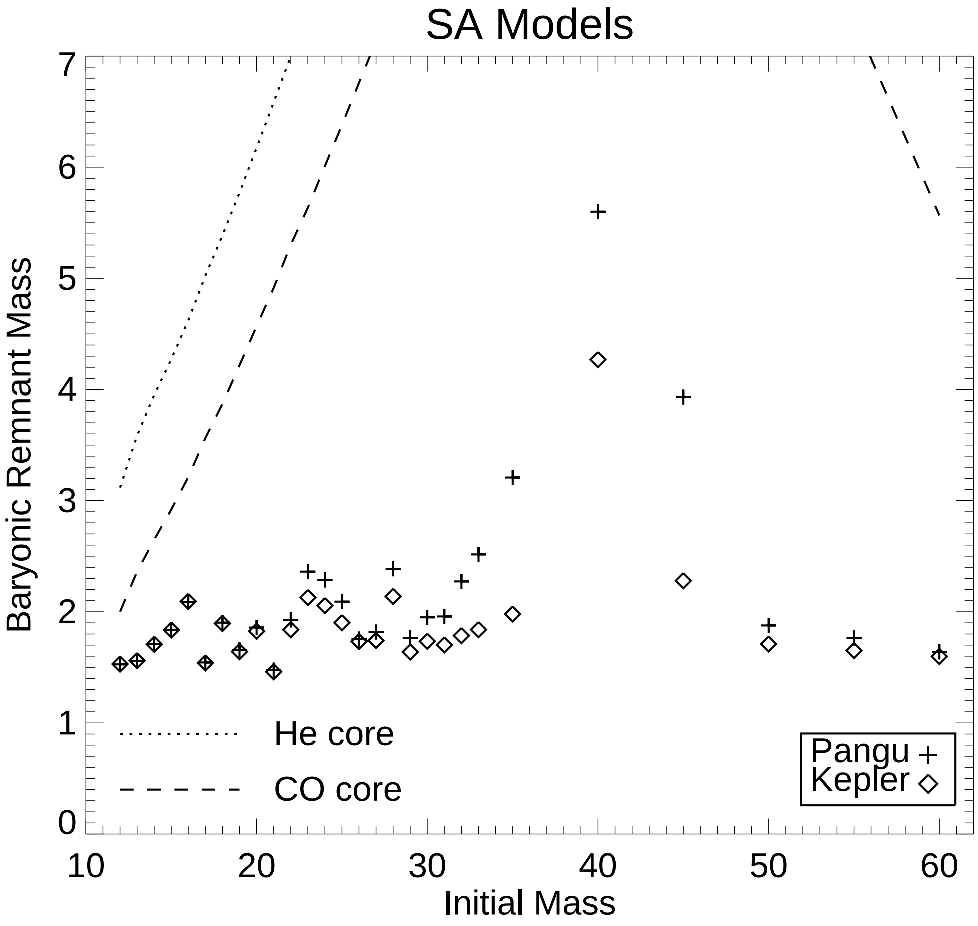

Fig. 9.— Comparison of baryonic remnant masses for SA series with Kepler and Pangu. The results from two different codes are similar. However, the final baryonic remnant masses calculated using Pangu (plus symbols) are greater than those calculated using Kepler (diamond symbols), especially for the initial mass range of $30 - 50\,\mathrm{M}_{\odot}$.

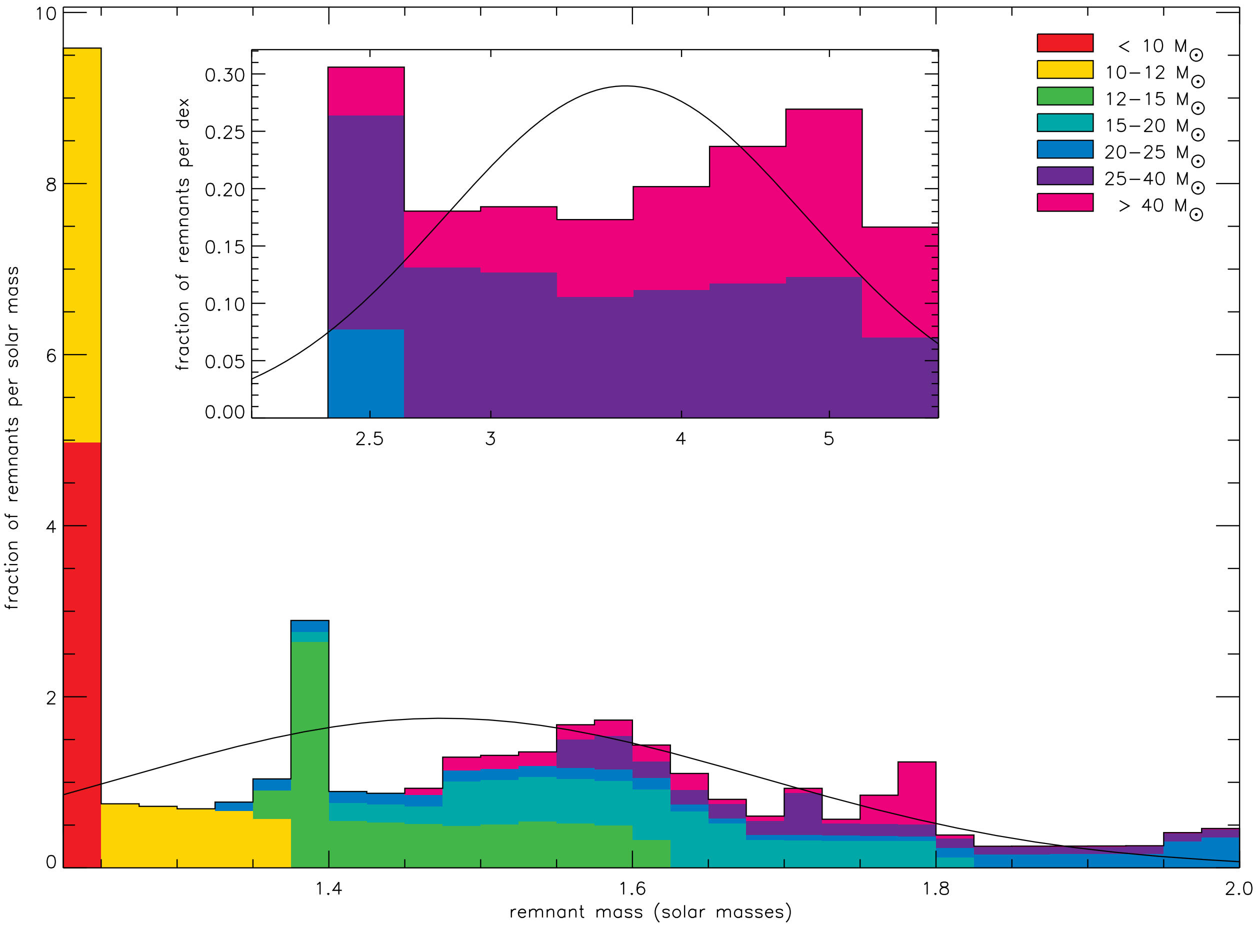

Fig. 10.— Distribution of remnant masses for 1.2 B explosions of solar metallicity stars with pistons located at the entropy $S/N_Ak = 4$ point for an initial mass range of $9.1\,M_\odot$ to $100\,M_\odot$. We assumed a maximum neutron stars mass of $2\,M_\odot$. The main figures shoes the *gravitational* masses of neutron stars, the insert shows the *baryonic* masses of black holes. The color coding (cumulative) indicates the initial mass range of the progenitor stars. The curve is a Gaussian fit with the same average and variance as distribution for the neutron stars (main figure). For the insert the curve is a Gaussian fit to the logarithm of black hole masses (geometric fit). The normalization of the bins in the big plot is such that the sum over the bins times the bin width equals total fraction of neutron stars. For the inserts the normalization is not "per solar mass" but "per dex", i.e., the sum of bin height times bin width in dex equals the total fraction of black holes. The bin sizes are $0.025\,M_\odot$ for the main figure and 0.05 dex for the insert.

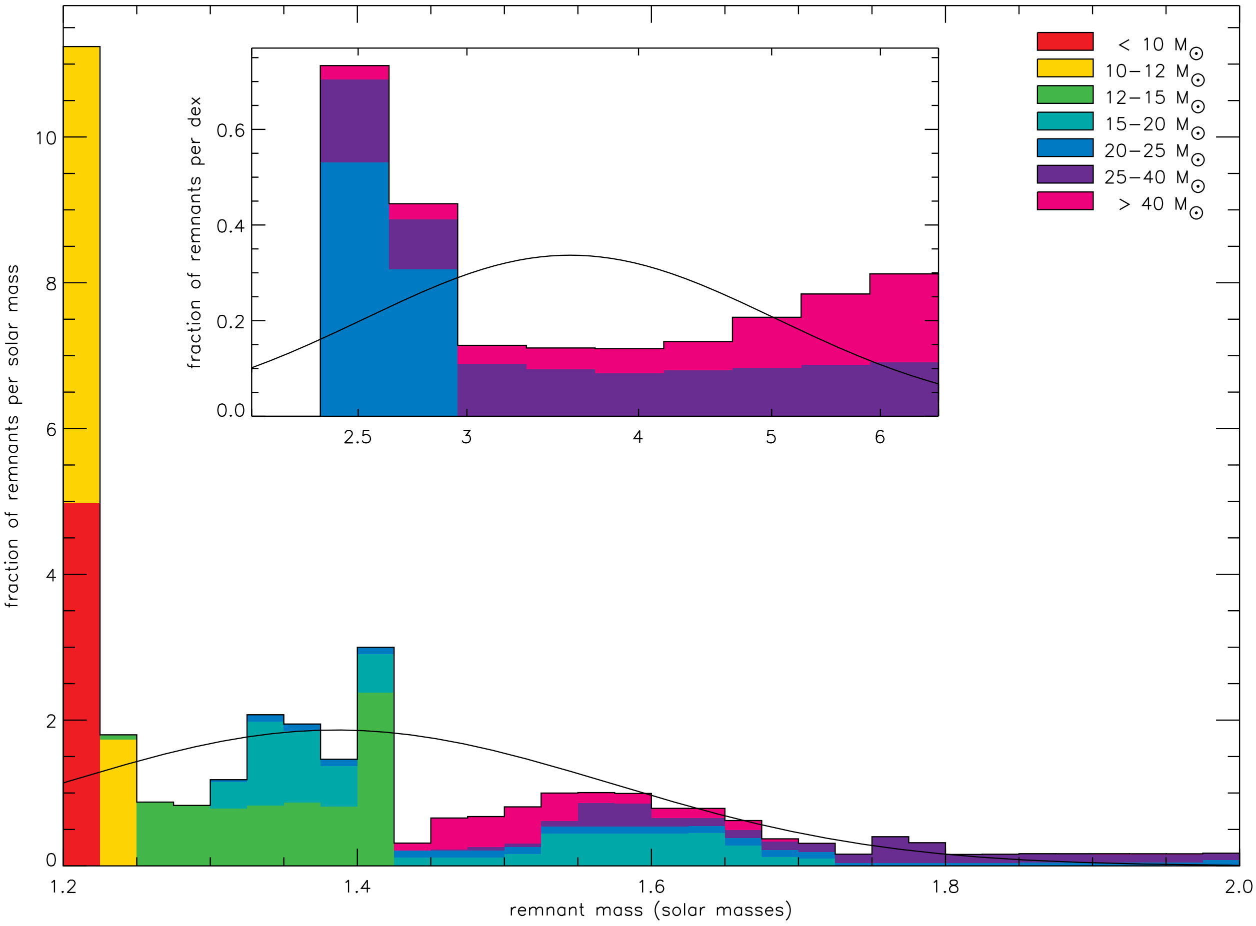

Fig. 11.— Distribution of remnant masses for 1.2 B explosions of solar metallicity stars with pistons located at the edge of the deleptonized core, for an initial mass range of 9.1 M$_\odot$ to 100 M$_\odot$, and an assumed maximum neutron star mass of 2 M$_\odot$. The main figure gives *gravitational* masses of neutron stars, the insert shows the *baryonic* masses of black holes. The color coding (cumulative) indicates the initial mass range of the progenitor stars. The curve is a Gaussian fit with the same average and variance as distribution for the neutron stars (main figure). For the insert the curve is a Gaussian fit to the logarithm of black hole masses (geometric fit). The normalization of the bins in the big plot is such that the sum over the bins times the bin width equals total fraction of neutron stars. For the inserts the normalization is not "per solar mass" but "per dex", i.e., the sum of bin height times bin width in dex equals the total fraction of black holes. The bin sizes are 0.025 M$_\odot$ for the main figure and 0.05 dex for the insert.